INVESTIGATION ON THE RELIABILITY OF EARTHQUAKE PREDICTION BASED ON IONOSPHERIC ELECTRON CONTENT VARIATION

A THESIS

SUBMITTED TO THE DEPARTMENT OF ELECTRICAL AND

ELECTRONICS ENGINEERING

AND THE GRADUATE SCHOOL OF ENGINEERING AND SCIENCE

OF BILKENT UNIVERSITY

IN PARTIAL FULFILLMENT OF THE REQUIREMENTS

FOR THE DEGREE OF

MASTER OF SCIENCE

By

Ali Alp Akyol

August, 2013

I certify that I have read this thesis and that in my opinion it is fully adequate, in scope and in quality, as a thesis for the degree of Master of Science.

Prof. Dr. Orhan Arıkan(Advisor)

I certify that I have read this thesis and that in my opinion it is fully adequate, in scope and in quality, as a thesis for the degree of Master of Science.

Assoc. Prof. Dr. Sinan Gezici

I certify that I have read this thesis and that in my opinion it is fully adequate, in scope and in quality, as a thesis for the degree of Master of Science.

Assist. Prof. Melih Çakmakcı

Approved for the Graduate School of Engineering and Science:

Prof. Dr. Levent Onural
Director of the Graduate School

ABSTRACT

INVESTIGATION ON THE RELIABILITY OF EARTHQUAKE PREDICTION BASED ON IONOSPHERIC ELECTRON CONTENT VARIATION

Ali Alp Akyol
M.S. in Electrical and Electronics Engineering
Supervisor: Prof. Dr. Orhan Arıkan
August, 2013

Ionosphere region of Earth's upper atmosphere ranging from 90 km to 1000 km altitude, has a significant effect on military and civilian communications, satellite communications and positioning systems. Solar, geomagnetic, gravitational and seismic activities cause variations in the electron distribution of the atmosphere. The number of electrons within a vertical column of 1 m^2 cross section, which is called as Total Electron Content (TEC), is a measurable feature of the ionosphere that provides valuable information about the ionosphere. TEC can be measured fast and accurately by using the phase difference between transmitted satellite positioning signals such as in the Global Positioning System (GPS).

To investigate the reliability of earthquake prediction based on detection of local ionospheric anomalies, TEC measurements obtained from a network of GPS receivers over a period of 2 years in 2010 and 2011 are used to generate detection signals. For a day of interest, after selecting a receiver station surrounding GPS stations that are located within 150 km of the chosen station used to estimate TEC measurements at the chosen station. In one of the proposed techniques, detection of ionospheric anomalies is based on distance between measured TEC and its estimate. Detection threshold is obtained based on statistical variation of this distance for the days with insignificant seismic activities. Also, another detection technique based on temporal variation of TEC measurements is proposed. Both individual and fused detection performances of these techniques are investigated for a given level of false alarms. It is observed that the fused detection has superior performance and able to detect 15 out of 23 earthquakes of magnitude larger than 5 in Richter scale while generating 8 false alarms.

Keywords: Total Electron Content (TEC), Global Positioning System (GPS).

ÖZET

İYONKÜRE ELEKTRON İÇERİĞİ KULLANILARAK DEPREM ÖNCÜL TESPİT BAŞARIMI İNCELENMESİ

Ali Alp Akyol
Elektrik ve Elektronik Mühendisliği Bölümü, Yüksek Lisans
Tez Yöneticisi: Prof. Dr. Orhan Arıkan
Ağustos, 2013

İyonküre, Dünya atmosferinin en dış tabakasının 90-1000 kmlik yükseklik aralığında yer almakta olup, askeri ve sivil haberleşme, uydu haberleşme ve konumlama sistemlerinin uygulanmasında çok önemli yere sahiptir. Atmosferin elektron dağılımı, Güneş etkinlikleri, jeomanyetik, yerçekimsel ve sismik hareketliliklerle değişiklikler gösterir. Ölçülebilen bir iyonosfer parametresi olan Toplam Elektron İçeriği (TEİ), metrekarelik dikey bir kesitte bulunan toplam elektron sayısına tekabül eder ve iyonosfer hakkında önemli bilgiler içermektedir. Yerküresel Konumlama Sisteminde (YKS) konumlama amaçlı kullanılan sinyaller arasındaki faz farkı kullanılarak iyonküre TEİ bilgisi pratik ve hızlı bir şekilde anlık olarak elde edilir.

Yerel iyonosferik değişiklikler kullanılarak deprem öncül tespit güvenilirliği incelenmesi amacıyla, TEİ ölçümleri 2010 ve 2011 yılları süresince bir YKS ağı kullanılarak elde edilmiş olup, deprem öncül tespit sinyali oluşturulmasında kullanılmıştır. Seçilen bir gün için, ağ üzerinde yer alan bir istasyon merkez alınarak oluşturulmuş 150 km yarıçaplı çember içerisinde kalan istasyonlar merkez istasyona ait TEİ ölçümünün kestirilmesinde kullanılmıştır. Önerilen bir teknik, iyonosferik anormalliklerin tespiti olup, TEİ ölçümleri ve TEİ kestirimleri arasındaki farkın kullanılmasına dayanmaktadır. Sismik aktivitenin olmadığı günler için bu fark kullanılarak deprem tahmin eşikleri elde edilmiştir. Ayrıca, TEİ ölçümlerinin zamansal değişimine dayanan başka bir tespit yöntemi önerilmiştir. Belirli bir yanlış alarm seviyesi için önerilen tekniklerin özgün ve birleşik tespit başarımları incelenmiştir. Birleşik tespit yönteminin başarımının diğer tekniklere göre üstün olduğu ve Richter ölçeğinde 5 şiddeti ve üzerinde meydana gelmiş 23 depremden 15 tanesini önceden tahmin ederken 8 yanlış alarm ürettiği gözlemlenmiştir.

Anahtar sözcükler: Toplam Elektron İçeriği (TEİ), Yerküresel Konumlama Sistemi (YKS).

Acknowledgement

First, I would like to thank my supervisors, Prof. Dr. Orhan Arıkan and Prof. Dr. Feza Arıkan, for their supervision, special guidance, suggestions, and support throughout my study. I would especially want to thank Orhan Arıkan for his invaluable encouragement and motivation through the development of this thesis.

I also thank Assoc. Prof. Dr. Sinan Gezici for his helps on the way of developing detection strategies, reading this thesis and being a member of my thesis committee. I would like to express my special thanks and gratitude to Assist. Prof. Melih Çakmakcı for accepting to read and review the thesis, and being a member of my thesis committee.

There are some friends who directly or indirectly contributed to my completion of this thesis. I thank my colleagues Fatih Emre Şimşek, Taha Ufuk Taşcı, Güneş Bayır, İsmail Uyanık for their understanding and support. I also thank my friends Ferman Kırkan, Serhan Taşcı, Seckin Bildik and Onur Taşoğlan for always being there to listen and motivate.

I am also appreciative of the financial and technical support from TUBITAK 109E055, Joint TUBITAK 110E296 and RFBR 11-02-91370-CTa and TUBITAK 112E568.

Finally, but forever I would express my thank to my parents, Mustafa and Melahat Akyol, for their love, encouragement and endless moral support.

Contents

List of Figures

List of Tables

Chapter 1

INTRODUCTION

Ionosphere is a region of Earths upper atmosphere ranging from 90 km to 1000 km altitude and ionized to a plasma as a result of mainly solar radiation affecting atoms and molecules in atmosphere. Ionospheric plasma is affected by several events such as solar radiation, geomagnetic storms and earthquakes. Figure 1.1, illustrates mid-latitude ionosphere profiles of plasma density and temperature. As shown Figure 1.1, temperature and plasma density vary with respect to altitude. When high correlation between plasmic density of ionosphere and electron concentration taken into consideration, it can be inferred that electron concentration also depends on altitude and the time of the day.

Ionosphere has strong effect on HF radio transmission and satellite communication systems. Therefore, it is important to monitor the plasma distribution in the ionosphere. As an example, strong solar radiation increases the ionospheres free electron content resulting with alterations in plasmic frequency and amount of reflection from the ionosphere both of which have significant impact on the quality of communications [1]. Satellite communication also suffer from the instantaneous state of the ionosphere that signals transmitted by satellites are affected by the dispersive and lossy ionospheric channel resulting with unreliable communications and disconnections [2].

Prior to strong earthquakes changes in cloud structures [3], temperature [4, 5,

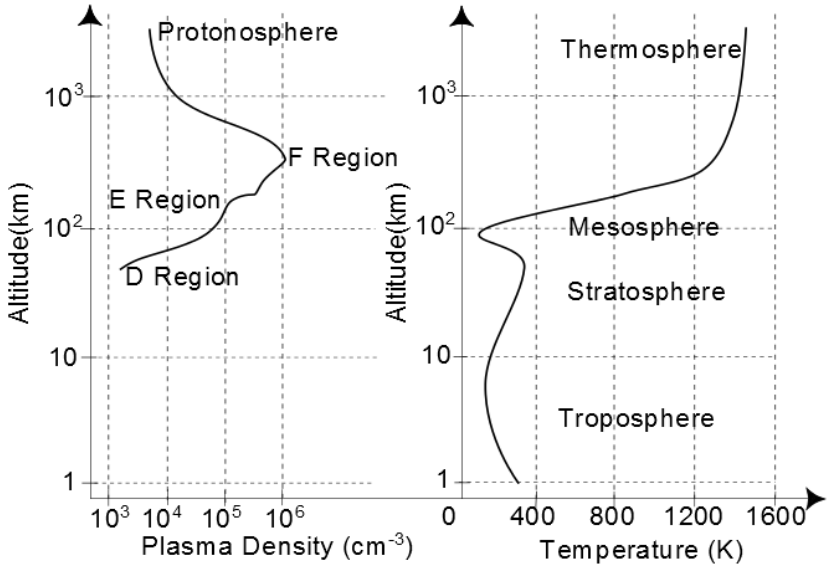

Figure 1.1: Ionospheric plasma density and atmospheric temperature with the layers illustrated.

6], strange lights [7] and abnormal animal behaviours [8] have been observed. Yet the observed changes might be triggered by geological or atmospherical incidences. Hence underlying mechanism between seismic activities and these changes are object of curiosity and remained unclear. Furthermore, earthquake precursors that are based on such changes might lead irrelevant and inconsistent detection results due to lack of statistical investigation and validation.

Recent studies have proposed links between seismic activities and state of the ionosphere. In one of the hypothesis, the observed local anomalies in the ionosphere is related to increased stress on the rock formations prior to the strong earthquakes which generates electrical current in the Earth's crust and ionize the air resulting local changes in the electron content of the ionosphere. In a laboratory experiment, significant amount of electrical current is induced on lateral surfaces of a granite slab by applying sufficiently high pressure on the top surface of the slab [9]. In the next stage of the experiment, pressure on the granite slab is increased leading to discovery of ionization in the air around the lateral surfaces of the slab. When the spatial extend of the fault lines and the tectonic pressure on these fault lines taken into consideration, it is a possibility that electrical currents that are sufficiently high to ionize the air and change the

state of the ionosphere can be induced. Furthermore, a coupling model for the stressed rock-Earth surface charges-atmosphere-ionosphere system is formulated based on these experimental results [10]. When electric fields and currents in the atmosphere are calculated and the ionospheric responses are simulated, current densities in the earthquake fault zone can cause Total Electron Content (TEC) variations of up to $2-25\%$ in daytime and $1-30\%$ in nighttime ionosphere.

Other studies shows that local ionospheric anomalies related to an earthquake can take place many days prior to the onset of the earthquake [11, 12, 13]. As an example, prior to the March 11, 2011 earthquake with magnitude 9 and the epicenter near the Tohoku region of Japan, ionosondes around Japan report ionospheric anomalies between March 3 and 11. It was observed that electron content of the ionosphere increased until 8 March and reached its maximum on this day [11]. In addition, observations that were made following the earthquake indicate that electron content of the ionosphere returned to its usual levels.

There have been many studies that attribute ionospheric variations to seismic activities [11, 14, 15, 16, 17, 18, 19, 20, 21, 22] by investigating ionospheric parameters such as ion temperatures, F2 layer critical frequency and TEC. During these investigations, statistical methods have been used for identifying the influence of seismic activities on ionospheric variations such as: TEC difference and variation analysis [14], ionospheric correction [15], correlation analysis between TEC and F2 layer critical frequency or different pairs of GPS receivers [16, 17, 18, 19], inter-quartile range and percentage analysis [20, 21, 22], TEC time derivative analysis [23] and relative deviation of daily ionospheric parameters from their corresponding monthly-median ones [24, 25]. Despite the fact that these statistical methods are applied to the major earthquakes with magnitude greater or equal than 6, investigated time duration and data sets are very limited. Hence long time reliability and robustness of such methods should be reassessed. Due to lack of statistical reliability analysis of earthquake precursors, earthquake prediction from ionospheric parameters is considered to be controversial. Considering the impact of a statistically reliable detection of earthquakes, an objective investigation of the probability of detection and probability of false alarm should be investigated. In this work, we will conduct such an investigation on the TEC

measurements of the ionosphere.

In order to obtain TEC measurements, positioning system networks such as Global Positioning System (GPS), GLONASS and TOPEX/Poseidon are widely used. TEC measurements can be obtained by phase difference of positioning signals transmitted by satellites to the positioning stations located on Earth. These local measurements of TEC can be used to obtain TEC maps by using spatial and temporal interpolation techniques [26]. In this study, the TEC measurement data has been obtained from Turkish National Permanent GPS Network (TNPGN-Active) consisting of 144 continuously-operating Global Navigation Satellite System (GNSS) stations.

In the first part of the thesis, the Turkish National Permanent GPS Network (TNPGN) is introduced and followed by illustration of sample TEC measurements in Section 2.1. In Chapter 2, a TEC based earthquake detection approach that consists of three different phases is proposed. In the first phase a novel spatio-temporal TEC interpolation technique [27] is used to provide estimates for measured TEC in a specific location based on measured TEC's in its neighbourhood in Section 2.2. The second phase employs local TEC variations around Turkey by identifying the distances between TEC measurements and TEC estimates with an appropriate distance metric. As introduced in Section 2.3, an earthquake detection signal that is sensitive to local TEC variations is constructed based on Symmetric Kullback-Leibler Distance (SKLD). Final phase of the proposed suggests two different earthquake detection thresholds for improved detection of a possible earthquake precursor in Section 2.4. Chapter 3 provides statistical performance characterization of the proposed detection technique. In order to improve the performance of the proposed temporal and spatial earthquake detectors, a fused version of them is proposed in Section 3.2. Also, nighttime performance of the proposed detection technique is investigated in Section 3.3. Finally, in Chapter 4, the thesis is concluded.

Chapter 2

PROPOSED TEC BASED EARTHQUAKE DETECTION APPROACH

In order to observe the current state of the Ionosphere, TEC parameter is widely used and obtained from positioning systems such as GPS, GLONASS and Topex/Poseidon. In this thesis, TEC measurements are obtained from Turkish National Permanent GPS Network (TNPGN) as introduced in Section 2.1. Due to inherent stochastic nature of the ionization taking place in the atmosphere, obtained TEC measurements show significant spatial and temporal variations as well. The detection of earthquake related anomalies in the ionosphere requires detection of local variations beyond the expected range of variation in the TEC measurements. In the proposed detection of these anomalies, there are three phases of processing. First, local TEC variations are estimated by using spatio-temporal estimation of available TEC measurements as in Section 2.2. Then, by using alternative variation metrics, detection signal is generated as presented in Section 2.3. Finally, in Section 2.4, generated detection signal is thresholded for declaring a detection by using a space-time adaptive detection threshold. In the following each of these stages will be detailed.

2.1 Turkish National Permanent GPS Network (TNPGN)

The TNPGN consists of 144 continuously-operating Global Navigation Satellite System (GNSS) stations which are distributed across Turkey and Turkish Republic of Northern Cyprus as in Figure 2.1. Since 2009, raw TEC data which are obtained by TNPGN are preprocessed by IONOLAB TEC service to obtain TEC measurements with a time separation of 2.5 minutes at each station in the network [28, 29].

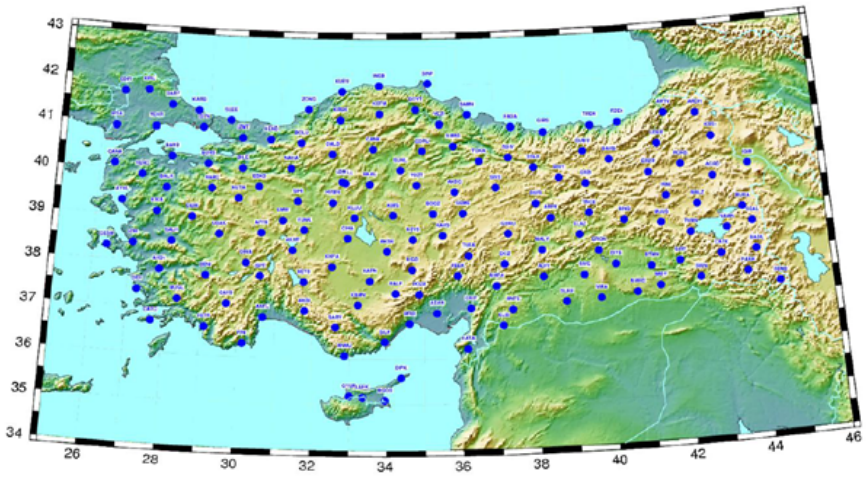

Figure 2.1: Positions of 144 TNPGN stations.

Note that recording continuous raw TEC data for all TNPGN stations is not possible due to positions of GPS satellites, power cuts, etc. Hence, the stations that contain available TEC measurements are determined for each given day and used for the generation of earthquake detection signals.

To illustrate available TEC data, in Figure 2.2, preprocessed daily TEC measurements at station with code name "deni" are shown for two different dates of 21.04.2010 and 23.04.2010, respectively. As seen in Figure 2.2, even the measurements are only two days apart, there is noticeable change in the recorded daily TEC values.

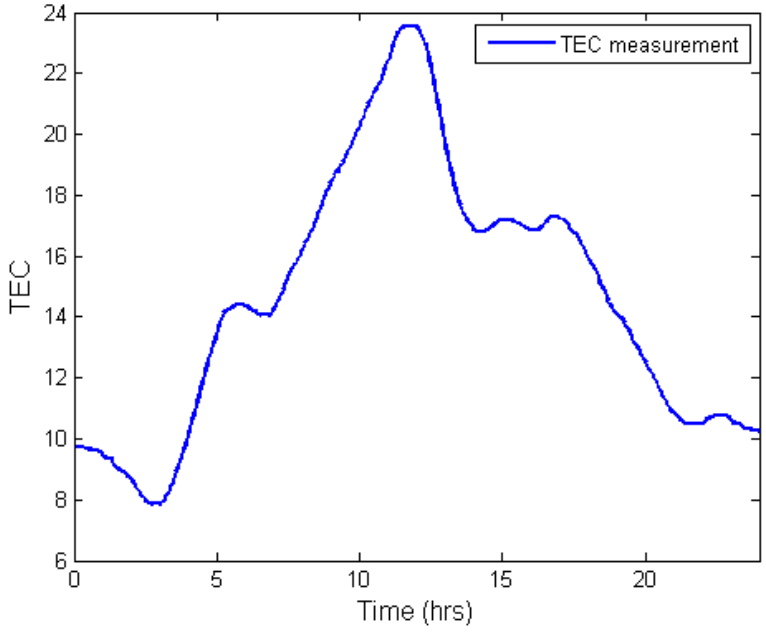

(a)

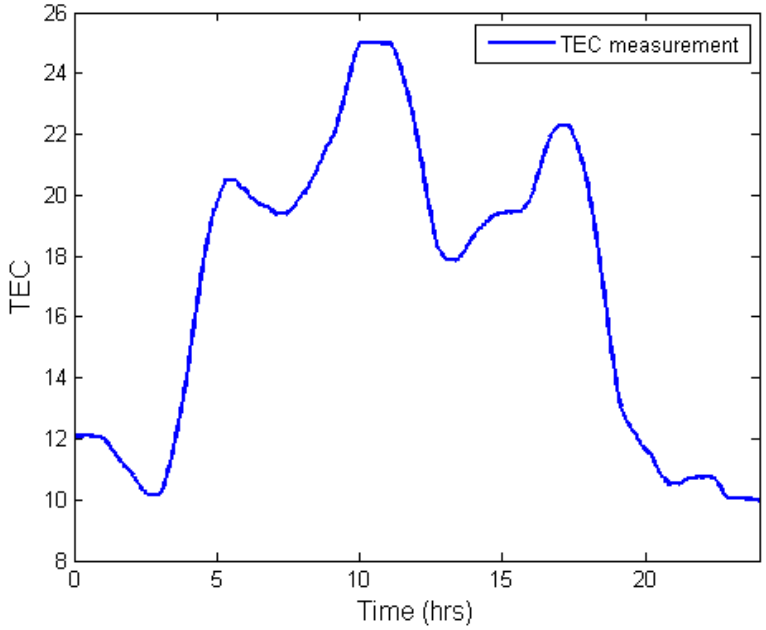

(b)

Figure 2.2: Daily TEC measurements at station "deni" on two different dates: (a) 21.04.2010 and (b) 23.04.2010.

2.2 A spatio-temporal TEC interpolation algorithm

Detection of a local anomaly in the ionosphere can be performed by generating an estimate for the TEC measurements obtained at a station based on the available measurements in the vicinity of this station (spatial estimation) or based on available measurements obtained in a time-window at the same station (temporal estimation) or both (spatio-temporal estimation). Here, we will focus on spatio-temporal estimation technique. Note that, the actual measurement and its spatio-temporally obtained estimate will be used to generate the detection signal.

For a chosen reference station u daily TEC measurement can be stacked to form a vector:

$$x_{u;d} = [x_{u;d}(1) \cdots x_{u;d}(n) \cdots x_{u;d}(N_{u;d})]^T, \tag{2.1}$$

$x_{u;d}(n)$, is the n^{th} TEC measurement in day d for a chosen reference station u. Parameter $N_{u;d}$ is the number of TEC measurements on day d. $[.]^T$ represents transpose. Parameter $N_{u;R_r}$ in (2.2) is the number of neighboring stations that are located within R_r km. radius when the selected center station u. Hence TEC estimate for the reference station u for day d can be obtained by its neighbors located within R_r km. radius, as in:

$$\hat{x}_{u;d;R_r} = \sum_{v=1}^{N_{u;R_r}} \alpha_{u;d;R_r}(v) x_{v;d;R_r}. \tag{2.2}$$

When reference station and day parameters are taken into consideration, parameter $\alpha_{u;d;R_r}(v)$ is the TEC measurement coefficient for the v^{th} neighboring station where $x_{v;d;R_r}$ represents this neighbors TEC measurement. In order to obtain, estimation coefficients $\alpha_{u;d;R_r}$, a temporal interpolation error minimization technique is implemented as in:

$$\min_{\alpha_{u;d;R_r}(v)} \sum_{d_i}^{d_s} \left\| x_{u;d_n} - \sum_{v=1}^{N_{u;R_r}} \alpha_{u;d;R_r}(v) x_{v;d_n;R_r} \right\|_2^2. \tag{2.3}$$

Equation (2.3) minimizes total estimation error over $[d_i, d_s]$ day range and results with optimum $\alpha_{u;d;R_r}(v)$ neighboring coefficients. Optimal solution to $\alpha_{u;d;R_r}$ can

be obtained in closed form as in (2.4):

$$\underline{\alpha}_{u;d;R_r} = \left(\sum_{d_n=d_i}^{d_s} X_{u;d_n;R_r}^T X_{u;d_n;R_r} \right)^{-1} \left(\sum_{d_n=d_i}^{d_s} b_{u;d_n;R_r} \right). \tag{2.4}$$

Note that, there exists a strong correlation between magnetic activity of the sun and the ionosphere. Sunspot number is a measure of the solar magnetic activity that it indicates possible state of the ionosphere. During this minimization process daily sunspot numbers are taken into consideration. The days within $[d_i, d_s]$ day range are clustered with respect to their corresponding sunspot number [30]. The days that are in the same cluster with selected day d are used during this minimization process. Therefore, minimization process is oriented with the daily sunspot number and error between TEC measurement and TEC estimate caused by solar magnetic activity variation is reduced. $\underline{\alpha}_{u;d;R_r}$ has the closed form as in (2.5), representing the vector of optimum coefficients for the neighbors located within R_r km. radius when chosen reference station is u and chosen day d:

$$\underline{\alpha}_{u;d_n;R_r} = [\alpha_{u;d_n;R_r}(1) \cdots \alpha_{u;d_n;R_r}(v) \cdots \alpha_{u;d_n;R_r}(N_{u;R_r})]^T. \tag{2.5}$$

For a reference station u and a chosen day d_n, $X_{u;d_n;R_r}$ in (2.4) is constructed by stacking TEC measurements of R_r km. neighbouring stations as:

$$X_{u;d_n;R_r} = [x_{1;d_n;R_r} \cdots x_{v;d_n;R_r} \cdots x_{N_{u;R_r};d_n;R_r}]. \tag{2.6}$$

Furthermore, vector $b_{u;d_n;R_r}$ is defined as:

$$b_{u;d_n;R_r} = X_{u;d_n;R_r}^T x_{u;d_n} \ , \tag{2.7}$$

which contributes to the calculation of $\underline{\alpha}_{u;d_n;R_r}$ as in (2.4).

Finally, TEC estimate $\hat{x}_{u;d;R_r}$ can be calculated by using TEC measurements of it's N_{u,R_r} neighbours as mentioned in (2.2). Hence, it becomes possible to identify TEC variations by comparing TEC estimate $\hat{x}_{u;d;R_r}$ and TEC measurement $x_{u;d}$ for a reference station u, for a day d and for a radius R_r.

In order to illustrate the interpolation performance, among 144 TNPGN stations, "deni" station, which is located near "Denizli" in the western Turkey, is

chosen as the reference station. The 9 neighboring stations that are located within 150 kms of "deni" are used in spatio-temporal estimation for the TEC measurement at "deni". Figure 2.3 illustrates both measured TEC measurements and their estimations for the same dates shown in Figure 2.2. Table 2.1, contains 9 neighboring stations with their optimal $\alpha_{u;d;R_r}$ coefficients obtained solving (2.3).

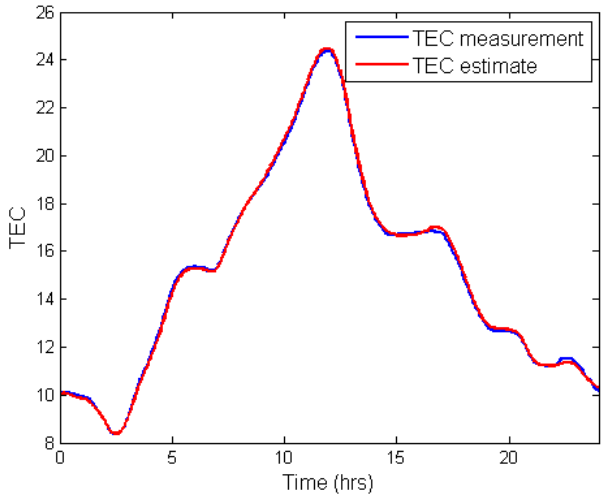

(a)

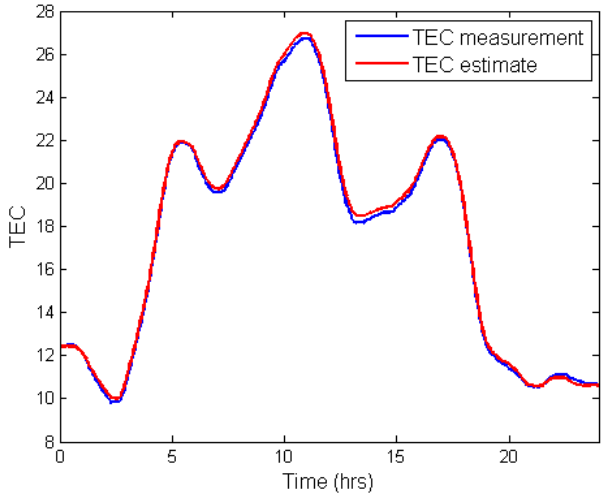

(b)

Figure 2.3: TEC measurements and estimates at station "deni" on two different dates: (a) 21.04.2010 and (b) 23.04.2010. Note that daily sunspot numbers for these two dates are 7 and 0, respectively.

As seen in Table 2.1, some neighboring stations do not have available TEC measurements for all the days of interest. For the date 21.04.2010 "usak" station

has no available TEC measurement. Hence neighboring coefficients are obtained only for the remaining 8 neighboring stations. For the date 23.04.2010 deir station has no available TEC measurement, however, "usak" station has available TEC measurement.

In order to determine the performance of estimation process, daily Root Mean Square (RMS) Error and Averaged Root Mean Square (ARMS) Error measures are calculated. Closed form expressions of RMS and ARMS are given in (2.8) and (2.9), respectively.

$$e_{RMS}(u;d;R_r) = \sqrt{\frac{1}{N_{u;d}} \left\| x_{u;d} - \hat{x}_{u;d;R_r} \right\|_2^2}, \tag{2.8}$$

$$e_{ARMS}(u;d;R_r) = \frac{1}{\left|d_i - d_s + 1\right|} \sum_{i=d_i}^{d_s} e_{RMS}(u;i;R_r), \tag{2.9}$$

where ARMS is obtained by averaging RMS over the days of $[d_i, d_s]$. In Table 2.1, the corresponding RMS and ARMS are shown in the second row. Unit for the representation of these two measures is the Total Electron Content unit (TECu) which is equal to 10^{16} electrons per meters squared.

Table 2.1: Estimation Errors and Estimation Coefficients for the minimization process at station "deni" on two different dates.

21.04.2010 "Denizli" Sunspot Number : 7		23.04.2010 "Denizli" Sunspot Number : 0	
e_{RMS} : $0.1603 TECu$	e_{ARMS} : $0.2875 TECu$	e_{RMS} : $0.2248 TECu$	e_{ARMS} : $0.1870 TECu$
Stations	$\alpha_{u;d;R_r}$	Stations	$\alpha_{u;d;R_r}$
cavd	0.0436	cavd	0.0147
mugl	0.4728	mugl	0.2203
dina	0.4409	dina	0.1956
ayd1	0.0402	ayd1	-0.0154
salh	0.0399	salh	0.2686
feth	-0.0048	feth	0.1261
ispt	0.1531	ispt	0.1626
deir	-0.1819	deir	-
usak	-	usak	0.0299

2.3 Generation of Earthquake Detection Signal

Symmetric Kullback-Leibler Distance (SKLD) is an appropriate metric for detecting local TEC variations accurately. SKLD is proposed for measuring the difference between two Probability Density Functions (PDFs) [31, 32, 33]. Since TEC measurement and TEC estimate always take positive TEC values, they can be converted into PDFs by normalization given in (2.10) and (2.11), respectively [34, 35]:

$$P_{u;d} = x_{u;d}\left(\sum_{n=1}^{N_{u;d}} x_{u;d}(n)\right)^{-1}, \tag{2.10}$$

$$\hat{P}_{u;d;R_r} = \hat{x}_{u;d;R_r}\left(\sum_{n=1}^{N_{u;d}} \hat{x}_{u;d;R_r}(n)\right)^{-1}. \tag{2.11}$$

By using (2.10) and (2.11), Kullback-Leibler Distance (KLD) from $\hat{P}_{u;d;R_r}$ to $P_{u;d}$ can be calculated as in (2.12) and KLD from $P_{u;d}$ to $\hat{P}_{u;d;R_r}$ can also be calculated as in (2.13), respectively:

$$KLD(\hat{P}_{u;d;R_r}|P_{u;d}) = \left(\sum_{n=1}^{N_{u;d}} \hat{P}_{u;d;R_r}(n) ln\left(\frac{\hat{P}_{u;d;R_r}(n)}{P_{u;d}(n)}\right)\right), \tag{2.12}$$

$$KLD(P_{u;d}|\hat{P}_{u;d;R_r}) = \left(\sum_{n=1}^{N_{u;d}} P_{u;d}(n) ln\left(\frac{P_{u;d}(n)}{\hat{P}_{u;d;R_r}(n)}\right)\right). \tag{2.13}$$

By adding (2.12) and (2.13), SKLD between any given TEC measurement and its estimate can be obtained as:

$$SKLD(P_{u;d}; \hat{P}_{u;d;R_r}) = KLD(\hat{P}_{u;d;R_r}|P_{u;d}) + KLD(P_{u;d}|\hat{P}_{u;d;R_r}). \tag{2.14}$$

Earthquake detection signal which can represent local TEC variations is constructed by calculating SKLD for all available stations in TNPGN and for all days on which TNPGN stations are operational. For a given day, SKLDs can

be calculated for available stations and represented as a 2-D map by two dimensional Kriging interpolation [36, 37]. Hence, an earthquake detection signal or surface can be constructed by kriging all available SKLD calculations for a given day. Figure 2.4 illustrates a generated earthquake detection signal for two different dates: 19.10.2011 and 20.10.2011. As seen in the Figures, the generated detection signal has both temporal and spatial variation.

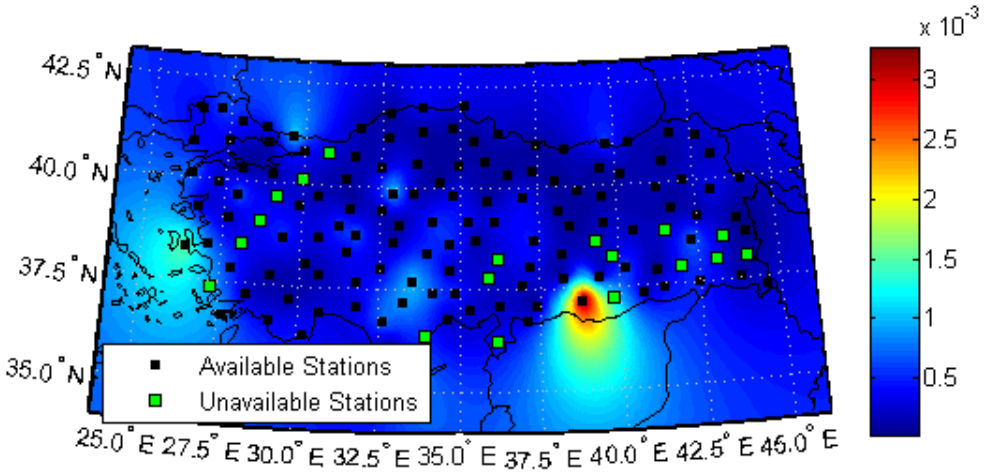

(a)

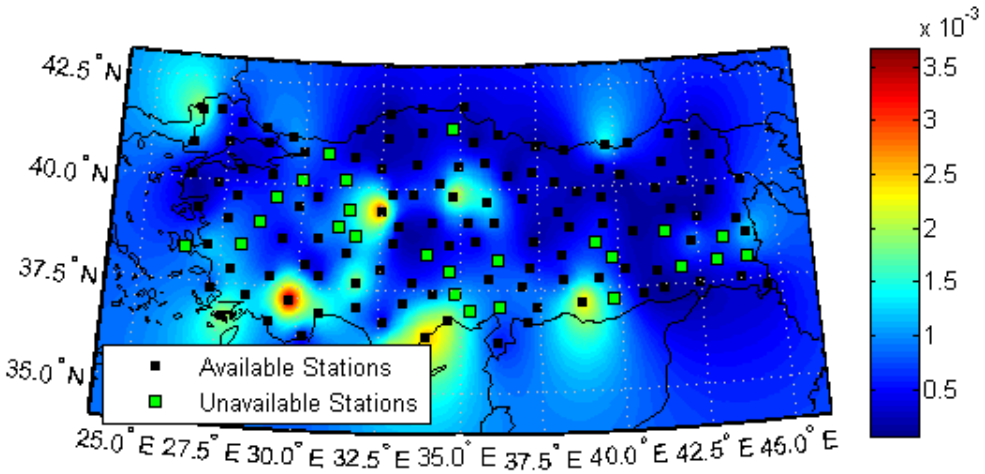

(b)

Figure 2.4: Visualization of earthquake detection signal for two different dates: (a) 19.10.2011 and (b) 20.10.2011.

2.4 Earthquake Detection Thresholds

On the generated earthquake detection signal, thresholding can be used to identify local anomalies beyond the expected range of variations. The detection thresholds can be chosen as: constant in time but varying in space (spatial thresholds) or constant in space and vary in time (temporal thresholds) or vary in both space and time (spatio-temporal thresholds). In this thesis, spatial earthquake detection thresholds and temporal earthquake detection thresholds are generated by statistical analysis of the false alarms. In order to generate an earthquake detection threshold for a given value of false alarm rate, days at which possible seismic activity takes place should be extracted from the data to obtain no seismic activity class of days. In this thesis, spatial earthquake detection thresholds which do not vary in time are generated by using no seismic activity class. Therefore, these thresholds can detect beyond the expected local TEC variations for the seismic activity class. Temporal earthquake detection thresholds are generated by using both seismic and no seismic activity classes. In Section 2.4.1 and Section 2.4.2, generation of spatial and temporal earthquake detection thresholds will be detailed.

2.4.1 Spatial earthquake detection thresholds

Spatial earthquake detection thresholds are generated by estimating a negative Pareto cumulative distribution for local TEC variations at each TNPGN stations on the days with no seismic activity [38]. Due to estimated negative cumulative distributions, TEC variation thresholds are obtained by choosing a certain tail probability among estimated local TEC variation probabilities for each station individually.

Since TEC measurements and TEC estimates always take positive TEC values, choosing a truncated distribution is reasonable to restrict the observation domain of interest to positive values. By using upper truncated Pareto distributional models, dense TEC datasets are observed to follow a power law probability

tail for large values of TEC measurements. Therefore, maximum likelihood based distribution estimations can be used for accurate tail estimation for truncated models with power law tails.

If W is a random variable with Pareto distribution, then its probability distribution function is given by [39]:

$$P(W > w) = \gamma^{\alpha} w^{-\alpha} = \left(\frac{\gamma}{w}\right)^{\alpha},\ w \geq \gamma > 0\ and\ \alpha > 0. \tag{2.15}$$

As indicated in (2.15), negative cumulative distribution function depends on γ and α parameters. When upper-truncated Pareto random variable X taken into consideration, it depends on γ, υ, α parameters and has a negative cumulative distribution as in [40]:

$$1\ -\ F_X(x)\ = P(X > x) = \frac{\gamma^{\alpha}(x^{-\alpha}\ -\ \upsilon^{-\alpha})}{1\ -\ \left(\frac{\gamma}{\upsilon}\right)^{\alpha}}\ ,\ 0 < \gamma \leq x \leq \upsilon < \infty\ . \tag{2.16}$$

These γ, υ and α parameters can be estimated by using maximum likelihood estimation to form negative cumulative distribution function. For a reference station u and n seismically inactive days, local TEC variations can be sorted as:

$$T_u\ =\ [T_u(1) \cdots T_u(i) \cdots T_u(n)]\ , \tag{2.17}$$

in descending order. When maximum likelihood estimates for $\hat{\gamma}$ and $\hat{\upsilon}$ parameters are chosen as:

$$\hat{\gamma}\ =\ T_u(n)\ =\ \min(T_u(1)\ ,\ T_u(2)\ ,\ \cdots\ ,\ T_u(n))\ , \tag{2.18}$$

$$\hat{\upsilon}\ =\ T_u(1)\ =\ \max(T_u(1)\ ,\ T_u(2)\ ,\ \cdots\ ,\ T_u(n))\ , \tag{2.19}$$

maximum likelihood estimate for α is obtained as the solution to:

$$\frac{n}{\hat{\alpha}}\ +\ \frac{n\left(\frac{\hat{\gamma}}{\hat{\upsilon}}\right)^{\hat{\alpha}} ln\left(\frac{\hat{\gamma}}{\hat{\upsilon}}\right)}{1\ -\ n\left(\frac{\hat{\gamma}}{\hat{\upsilon}}\right)^{\hat{\alpha}}}\ -\ \sum_{i=1}^{n}\left[ln(T_u(i))\ -\ ln(\hat{\gamma})\right]\ =\ 0\ . \tag{2.20}$$

Finally, upper-truncated Pareto negative cumulative distribution function is estimated by using $\hat{\gamma}$, $\hat{\upsilon}$ and $\hat{\alpha}$ parameters in (2.16), [38]. Hence, probability of a

local TEC variation that observed in any given TNPGN station can be estimated for seismically inactive days. To demonstrate estimation, seismically active days are extracted from days in between 2011 and 2012. Days of which an earthquake with magnitude greater or equal than 5 and 9 days prior to these earthquakes are marked as seismically active days. Figure 2.5 illustrates estimated upper-truncated Pareto negative cumulative distribution functions by using seismically inactive days for two TNPGN stations : "Ankara" and "Denizli".

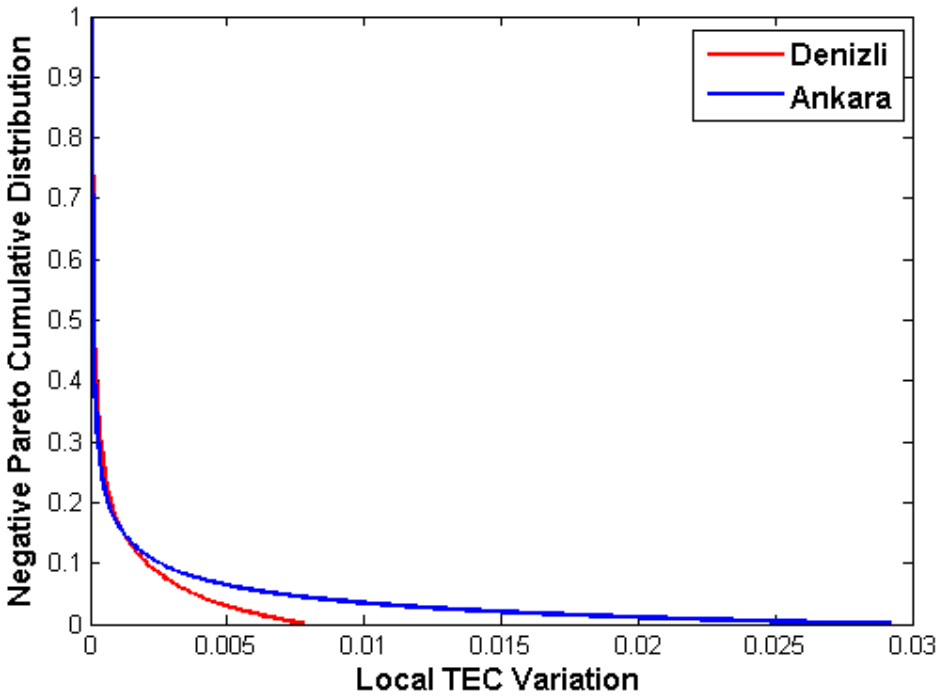

Figure 2.5: Local TEC variation Negative Pareto cumulative distributions for "Denizli" (red) and "Ankara" (blue) stations.

As seen in Figure 2.5, estimated upper-truncated Pareto negative cumulative distribution functions are different for "Ankara" and "Denizli" stations. For a given tail probability of local TEC variation around 0.05, local TEC variations observed at "Denizli" and "Ankara" stations are 0.005 and 0.01, respectively. When whole TNPGN is taken into consideration, every station on the TNPGN has different estimated negative Pareto cummulative distribution functions and takes different local TEC variation values for a particular local TEC variation probability. Therefore, it is possible to generate a spatial earthquake detection

threshold by choosing a certain tail probability among estimated local TEC variation probabilities and choosing corresponding local TEC variations as thresholds. Figure 2.6, illustrates three different spatial earthquake detection thresholds generated based on the statistics obtained from the no seismic activity days in 2011 and 2012. Tail probability of local TEC variation is chosen as 0.01 in Figure 2.6a, 0.005 in Figure 2.6b, and 0.001 in Figure 2.6c for each station individually.

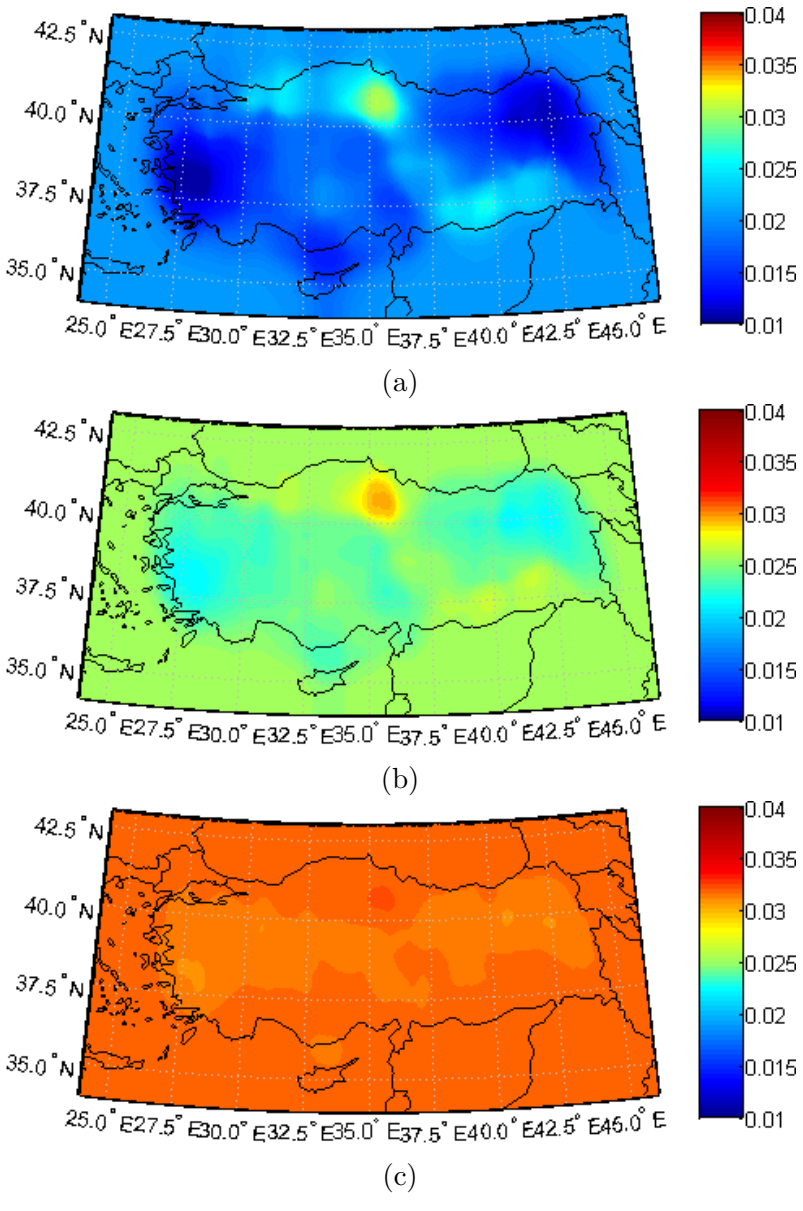

(a)

(b)

(c)

Figure 2.6: Three different spatial earthquake detection thresholds with their local TEC variation tail probabilities: (a) 0.01, (b) 0.005, and (c) 0.001.

As illustrated in Figure 2.6, these spatially varying earthquake detection thresholds have different local TEC variation mean values due to their different local TEC variation tail probabilities. A spatial earthquake detector that can control false alarm probability based on spatial earthquake detection thresholds will be presented in Section 2.5.

2.4.2 Temporal earthquake detection thresholds

Temporal earthquake detection thresholds are generated by calculating median and standard deviation of all local TEC variations obtained by TNPGN stations for both seismic and no seismic activity classes individually. Threshold for a given day is obtained by adding total TEC variation median with a constant multiple of its standard deviation. Temporal earthquake detection threshold TET_d for a given day can be obtained as in:

$$TET_d \;=\; M_d \;+\; \beta S_d \;, \tag{2.21}$$

where M_d is median and S_d is standard deviation of all TEC variations obtained by TNPGN stations for given day d. β parameter remains constant during the calculation of the TET_d as selected days d change. Figure 2.7, displays three different temporal earthquake detection thresholds generated for the 365 days in between 2011 and 2012 with β parameters: 0, 5, and 10. As seen in Figure 2.7, generated temporal earthquake detection thresholds vary in time and remains constant in space. Additionally, selecting higher β parameters results with higher local TEC variation thresholds for the days of interest.

A temporal earthquake detector that can control false alarm probability based on temporal earthquake detection thresholds will be presented in Section 2.5.

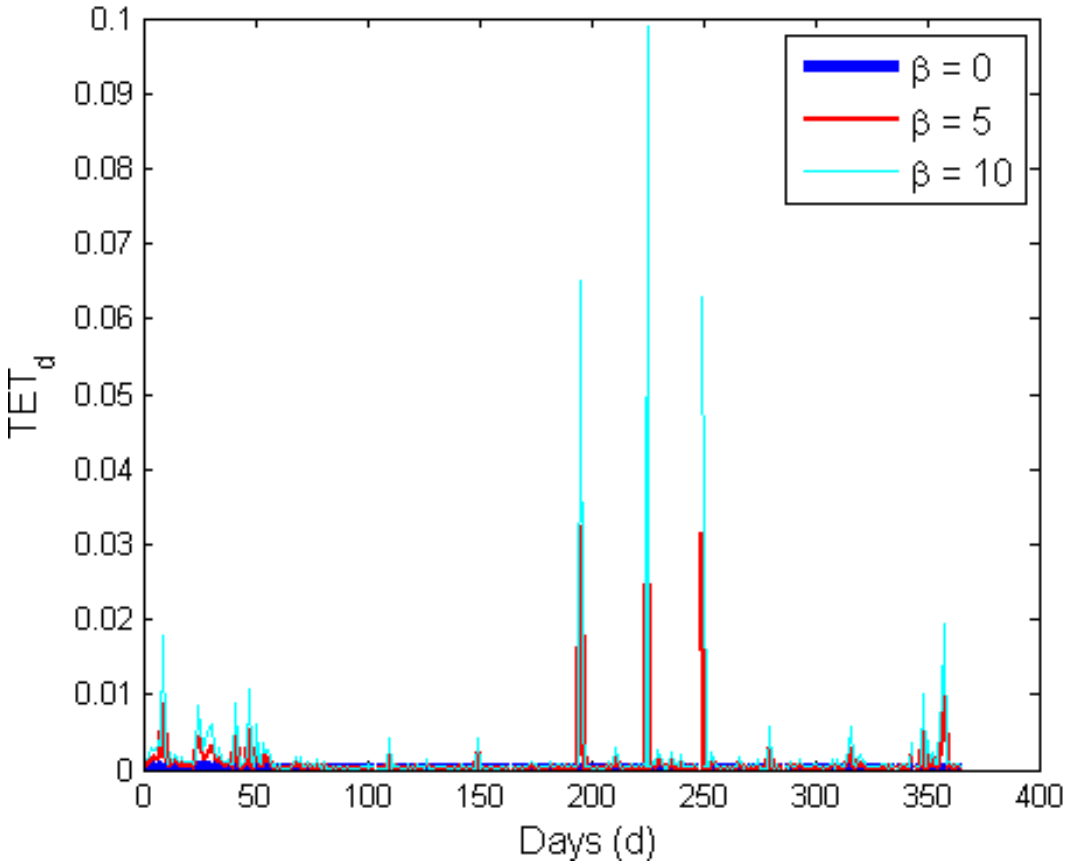

Figure 2.7: Three different temporal earthquake detection thresholds generated for the days in 2011 and 2012.

2.5 False Alarm Control

In order to generate false alarm probability controlling earthquake detectors, false alarm control performances of the earthquake detection thresholds are demonstrated. For the demonstration, days in 2011 are divided into two distinct classes: seismic activity and no seismic activity class as indicated in Section 2.4. Seismic activity class consists of 23 different time intervals including 9 days prior to the 23 earthquakes in Table 3.1 with earthquake days. Remaining 211 days are considered as in no seismic activity class.

Spatial earthquake detection thresholds are generated by using days of no seismic activity class only as discussed in Section 2.4.1. For a particular local TEC variation tail probability, every station on the TNPGN has different estimated

negative Pareto cummulative distribution functions and takes different local TEC variation thresholds as in Figure 2.5. Figure 2.8 depicts the relation between local TEC variation tail probability and probability of false alarm (P_{FA}) for the days in no seismic activity class. As seen in Figure 2.8, P_{FA} can be controlled by choosing different local TEC variation tail probabilities while generating spatial earthquake detection thresholds.

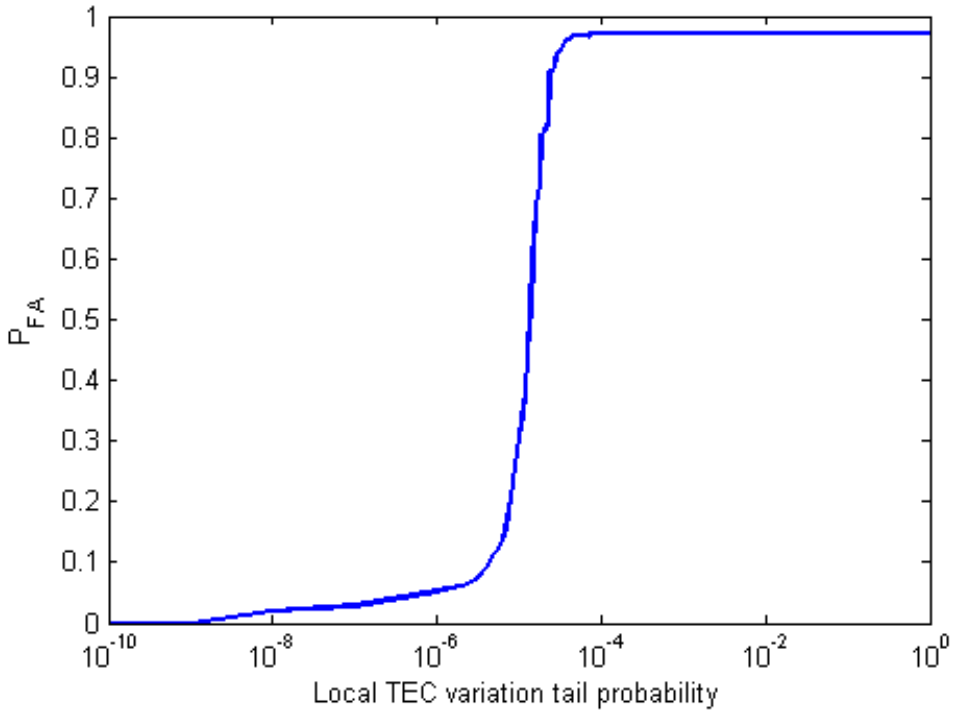

Figure 2.8: Adjusting P_{FA} by changing local TEC variation tail probability.

Unlike spatial earthquake detection thresholds, temporal earthquake detection thresholds are generated for everyday in 2011 regardless of days' class. Figure 2.9 depicts the relation between β parameter and P_{FA} generated for the days in no seismic activity class. As seen in the figure, P_{FA} can be controlled by choosing different β parameters while generating temporal earthquake detection thresholds.

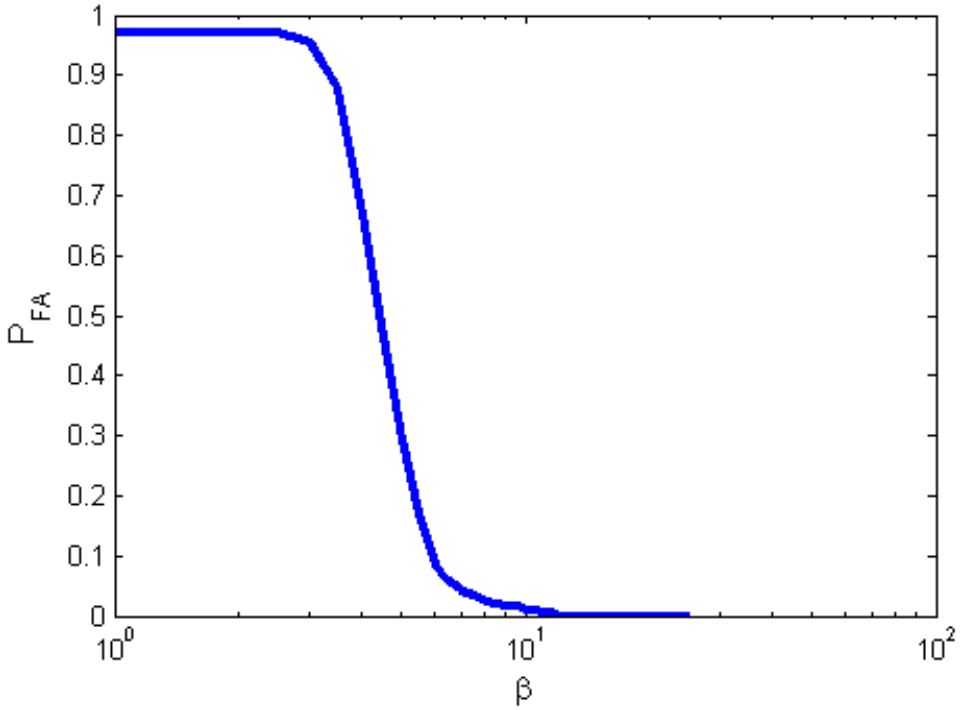

Figure 2.9: Adjusting P_{FA} by changing β parameter.

For a given P_{FA}, spatial and temporal earthquake detectors apply appropriate spatial and temporal earthquake detection thresholds to the generated earthquake detection signal by adjusting local TEC variation tail probability and β parameter, respectively. For a chosen day, when applied spatial or temporal earthquake detection thresholds are exceeded by any region of the earthquake detection signal, spatial or temporal detectors decide the exceedance as an upcoming earthquake. Earthquake predictions of detectors are resulted as false alarm if the chosen day belongs to seismic activity class and detection if the chosen day belongs to seismic activity class. Therefore, it is possible to identify probability of detection (P_D) of the generated detectors for any given P_{FA}.

Note that there are 10 distinct days of which no reliable TEC measurement is obtained by any TNPGN station due to circumstances discussed in Section 2.1. 6 of these days belong to the no seismic activity class and remaining 5 days belong to seismic activity class. Therefore, generated earthquake detectors operate for the P_{FA} ranging from 0 to 0.9716, as seen in Figure 2.8 and Figure 2.9.

In the following performance of the proposed earthquake detection approach will be demonstrated by applying spatial and temporal earthquake detectors to the earthquake detection signal generated for the days in between 2011 and 2012. Figure 2.10 visualizes flow diagram of proposed TEC based earthquake detection approach.

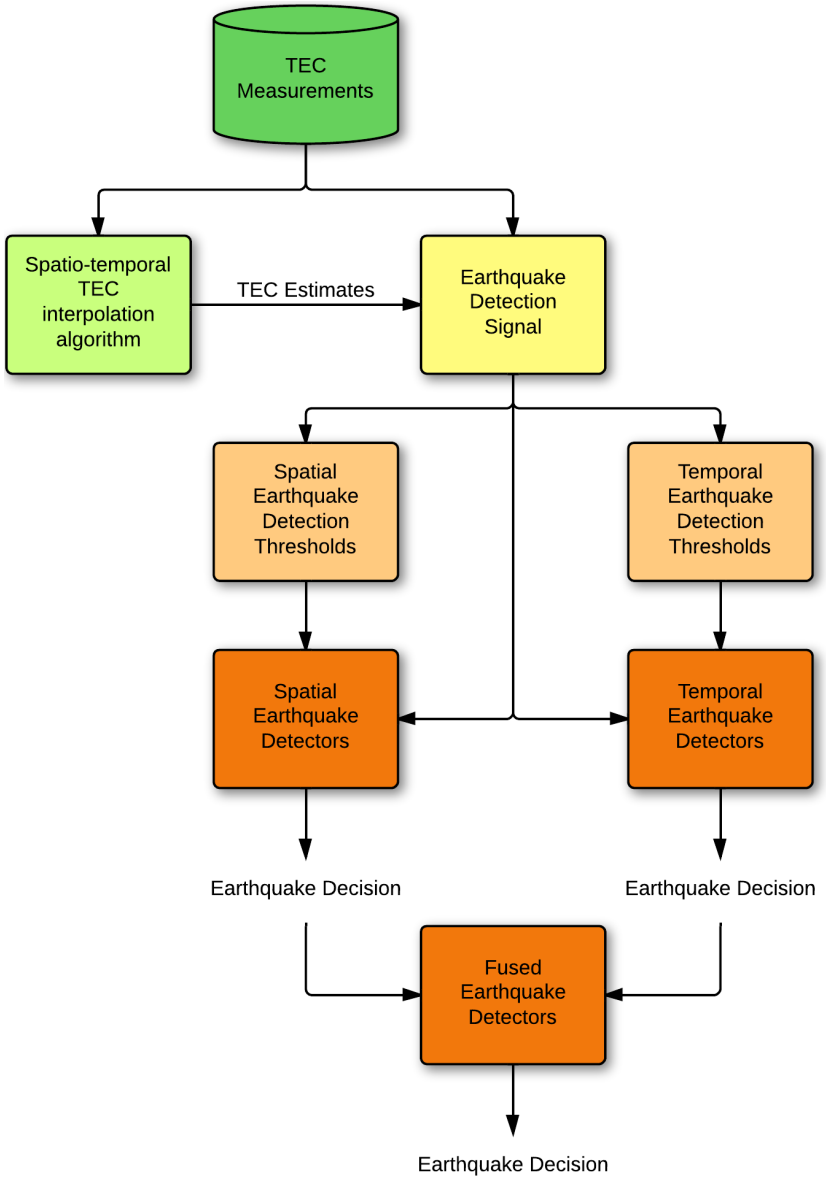

Figure 2.10: Flow diagram of proposed TEC based earthquake detection approach.

Chapter 3

PERFORMANCE OF THE PROPOSED TEC BASED EARTHQUAKE DETECTION APPROACH

To illustrate performance of the earthquake detection approach, 23 different earthquakes around Turkey of which had taken place in 2011 with magnitude greater than 5 in Richter scale are investigated. Table 3.1 summarizes the earthquakes in 5 different features in order: date, time, earthquake epicenter, earthquake magnitude in Richter and depth in km. In all simulations in subsequent sections, seismic activity class and no seismic activity class are divided with respect to these 23 earthquakes given in Table 3.1. During the performance evaluation, Receiver operating characteristic (ROC) curves of the proposed earthquake detectors are visualized. False alarm dates and regions with their TEC measurements and TEC estimates, detected earthquakes with their detection distance are illustrated for prediction results selected from ROC curves.

In this thesis, overall performance of the proposed earthquake detection approach is evaluated in two different earthquake detection signals: daytime and

Table 3.1: 23 different earthquakes around Turkey of which had taken place in 2011.

Date	Time	Earthquake Epicenter		Mw	Z
(dd.mm.yyyy)	(hh:mm)	Latitude	Longitude	(Richter)	(km)
19.01.2011	09:17	41.8770	42.7038	5.3	27.81
28.02.2011	07:49	34.7417	25.3913	5.5	25.42
01.04.2011	13:29	35.4819	26.4011	6.2	8.99
19.05.2011	20:15	39.1328	29.0820	5.7	24.46
23.06.2011	07:34	38.5562	39.6307	5.3	13.42
27.06.2011	21:13	39.1108	29.0260	5.0	18.27
25.07.2011	17:57	40.8195	27.7498	5.1	6.97
18.08.2011	14:57	42.3595	43.0042	5.0	15.5
13.09.2011	16:19	34.4090	23.7220	5.0	5.00
14.09.2011	03:35	37.2030	22.0120	5.0	35.05
22.09.2011	03:22	39.6597	38.6777	5.4	7.18
27.09.2011	12:08	34.1700	23.6200	5.2	40.43
10.10.2011	19:07	37.2050	22.0600	5.1	5.00
23.10.2011	10:41	38.6890	43.4657	6.7	19.02
24.10.2011	08:49	38.7060	43.5823	5.0	17.27
25.10.2011	14:55	38.8230	43.5857	5.4	17.44
27.10.2011	08:04	37.3807	43.8343	5.6	21.61
08.11.2011	22:05	38.7192	43.0778	5.4	8.36
09.11.2011	19:23	38.4382	43.2825	5.6	21.47
14.11.2011	22:08	38.7038	43.0833	5.1	23.32
18.11.2011	17:39	38.8022	43.8528	5.2	8.00
23.11.2011	12:18	35.4048	25.9317	5.0	6.96
30.11.2011	00:47	38.4700	43.2905	5.0	19.79

nighttime. Results obtained for both earthquake detection signals will be detailed in the following sections.

3.1 Daytime Results

To generate daytime earthquake detection signals, all available TEC measurements for all TNPGN stations are identified for days in 2011. TEC estimates for the TEC measurements are obtained by applying a novel spatio-temporal

interpolation algorithm. $[d_i\ d_s]$ day range is selected as 365 days during the minimization process as in Section 2.2. Finally, daytime earthquake detection signal is generated by measuring the distance between the TEC measurements and their TEC estimates with SKLD metric. Appropriate spatial and temporal earthquake detectors are applied to the generated earthquake detection signals. Figure 3.1 visualizes ROC curves of these two false alarm controlling detectors.

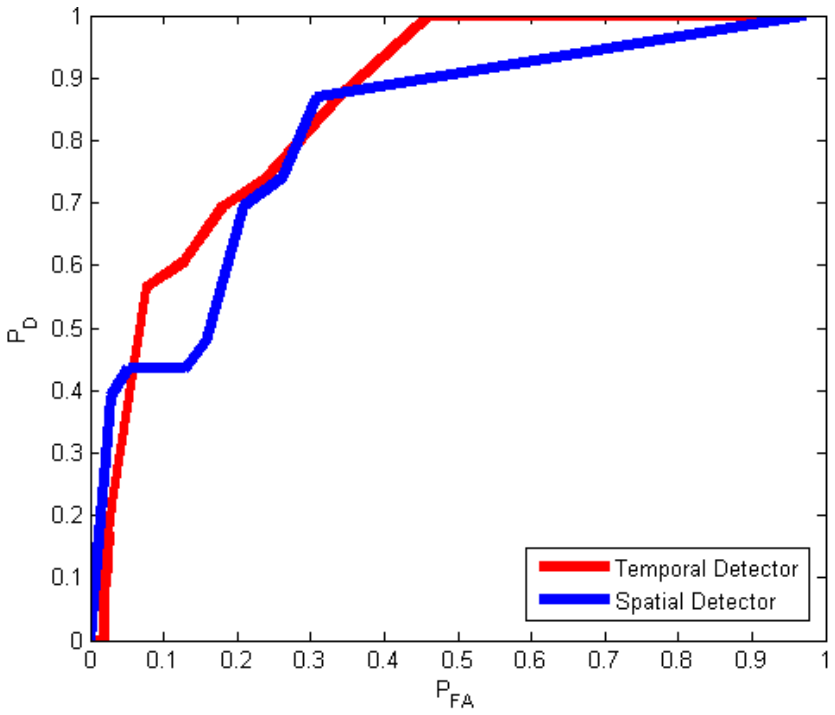

Figure 3.1: ROC curves of temporal (red) and spatial (blue) earthquake detectors for daytime earthquake detection signals.

As shown in Figure 3.1, spatial and temporal detectors have discriminative characteristics that their probability of detections $P'_D s$ are different for a given probability of false alarm P_{FA}. When P_{FA} is below 0.06 performance of the spatial detector precedes temporal detector. However, temporal detector outperforms spatial detector for any P_{FA} greater than 0.06 except 0.3. As a prediction result of temporal detector, the detector identifies 13 TEC anomalies prior to 23 earthquakes and gives false alarm for 16 out of 211 no seismic activity days. As a prediction result of spatial detector, the detector can identify 9 TEC anomalies prior to 23 earthquakes and gives false alarm for 6 out of 211 no seismic activity days. In second and third columns of Table 3.2, earthquake prediction results of

temporal and spatial detectors for daytime detection signal are given. Detected earthquakes are marked as "1"s and missed earthquakes are marked as "0"s in Table 3.2. Furthermore, locations of the 13 detected earthquakes are shown in Figure 3.2a and the 9 detected earthquakes are shown in Figure 3.2b.

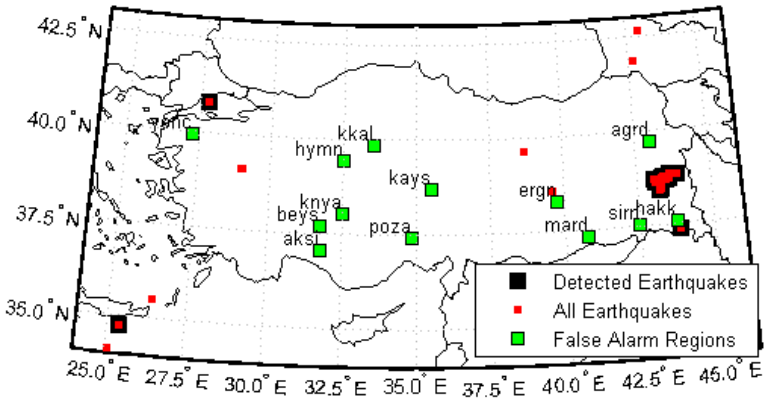

(a)

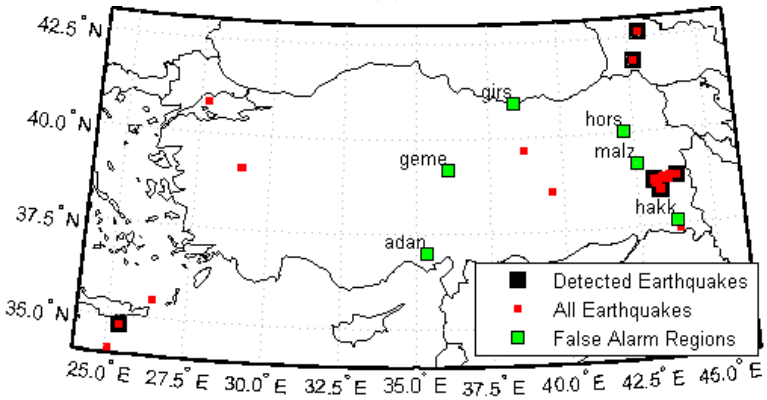

(b)

Figure 3.2: Detected earthquakes and False alarms for (a) temporal, (b) spatial earthquake detectors.

As seen in the Figure 3.2, detected earthquakes are gathered around certain regions of Turkey. Notice that some of the detected beyond the Turkish border. Since the distance between the measurement network and the epicenters are relatively close, this is an expected result [41, 42]. On the other hand, false alarms of spatial and temporal detectors are highly uncorrelated in both time and space. Therefore, there exists a possibility to reduce P_{FA} by combining spatial and temporal detectors. In the following section, detector fusion technique will be detailed with it's detection performance.

3.2 Detector Fusion

Detector fusion technique is based on generating a fused detector that combines outcomes of two or more detectors simultaneously that resulting outcome is in some sense better than would be possible when these outcomes were used individually [43]. Performance of the fused detector is highly depend on outcomes and numbers of combined detectors. In this thesis, spatial and temporal earthquake detectors are combined to form a fused detector for achieving higher performance in terms of lower false alarm and higher detection rates. To achieve that, one should consider combined detectors' characteristics: distribution of false alarms and coherence of detections. As illustrated in Figure 3.2, false alarms of spatial and temporal detectors are highly uncorrelated and scattered around Turkey. However, 7 out of 23 earthquakes are detected by both detectors as given in Table 3.2. Therefore, generating a fused detector that decides to an upcoming earthquake only when spatial and temporal detectors have the same earthquake decisions is able to eliminate scattered false alarms. The generated fused detector will have a pair of false alarm regions for days in no seismic activity class and a pair of detection regions for days in seismic activity class. Note that main concern of generating fused earthquake detectors is not to cover whole P_{FA} range but to enhance the performance of a selected prediction result obtained by combined detectors.

To demonstrate particular performance of proposed detector fusion technique, the daytime prediction result of temporal detector is selected as mentioned in Section 3.1. A fused detector is formed for comparing performance of the selected prediction result with fused detector prediction results. The fused detector outperforms the daytime temporal detector that a prediction result of the detector identifies 13 TEC anomalies prior to 23 earthquakes and gives false alarm for 8 out of 211 no seismic activity days. Figure 3.3 visualizes ROC curves for temporal, spatial and the fused detector. The compared earthquake prediction result of the fused detector is given in fourth column of Table 3.2. Additionally, it is possible to outperform the daytime prediction result of spatial detector mentioned in Section 3.1. 9 TEC anomalies prior to 23 earthquakes are identified with 5 false

alarms out of 211 no seismic activity days by forming another fused detector. The earthquake prediction result for this detector is given in fifth column of Table 3.2. As shown in Table 3.2, fused detectors detect the same earthquakes as temporal and spatial detectors while generating fewer number of false alarms.

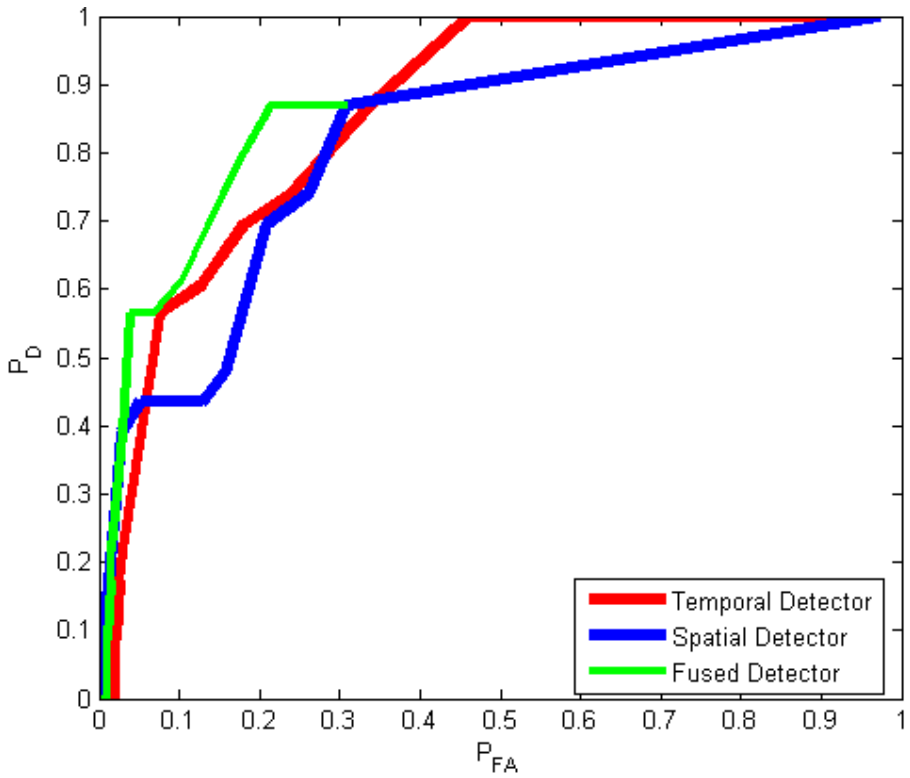

Figure 3.3: ROC curves of temporal (red), spatial (blue), and fused (green) earthquake detectors for daytime earthquake detection signals.

Figure 3.4 and Figure 3.5 illustrate TEC measurements and their estimates for 8 false alarm generating regions of the fused detector prediction result shown in Figure 3.3. For a false alarm day, fused detectors can generate two false alarms in different regions since, combined detectors can predict an earthquake at the same time but different regions. Figure 3.4 illustrates false alarms of combined temporal detector and Figure 3.5 illustrates false alarms of combined spatial detector for the date pairs of fused detector.

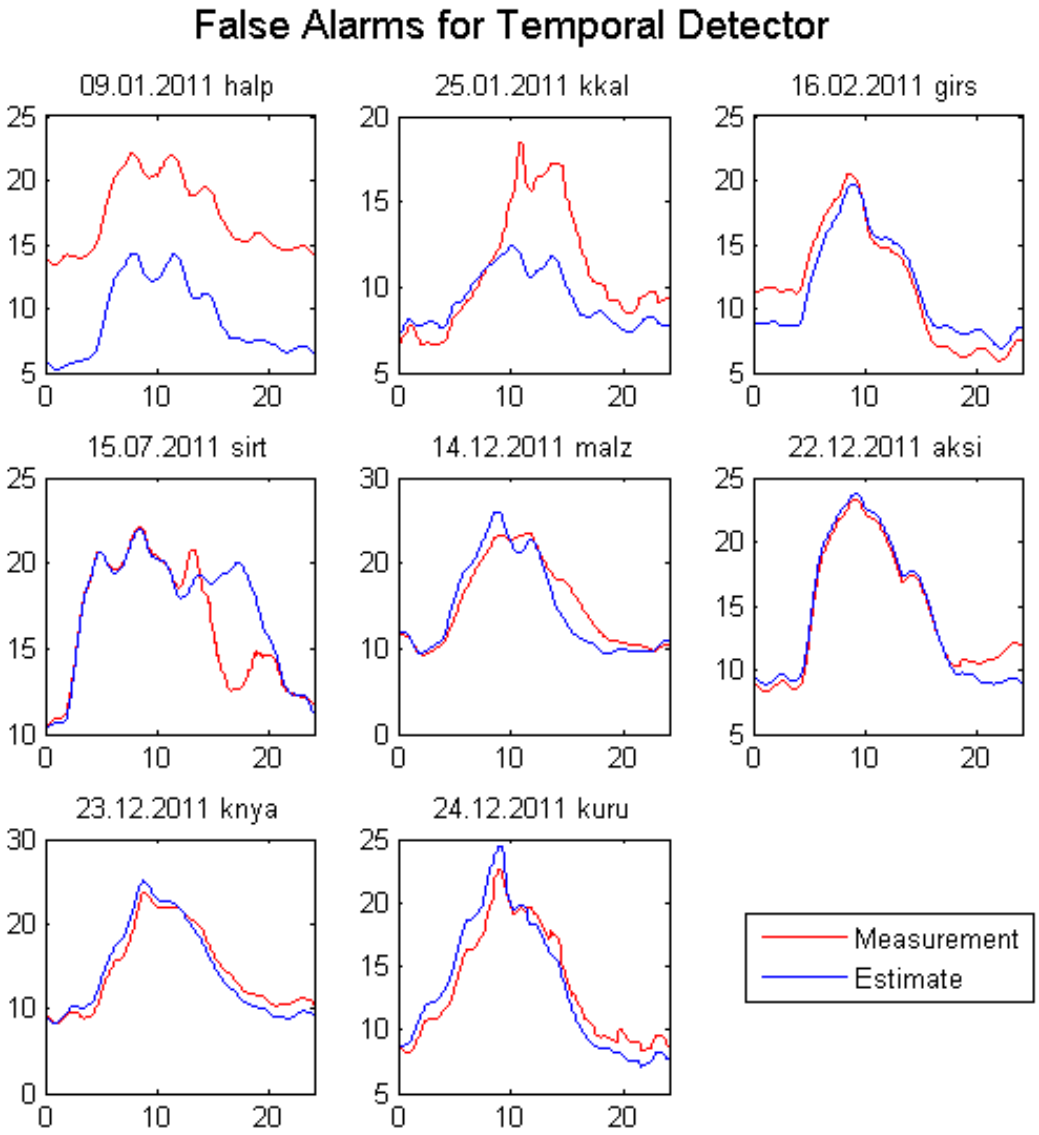

Figure 3.4: 8 different false alarm generating dates and regions: "halp", "kkal", "girs", "sirt", "malz", "aksi", "knya", and "kuru" for combined daytime temporal earthquake detector.

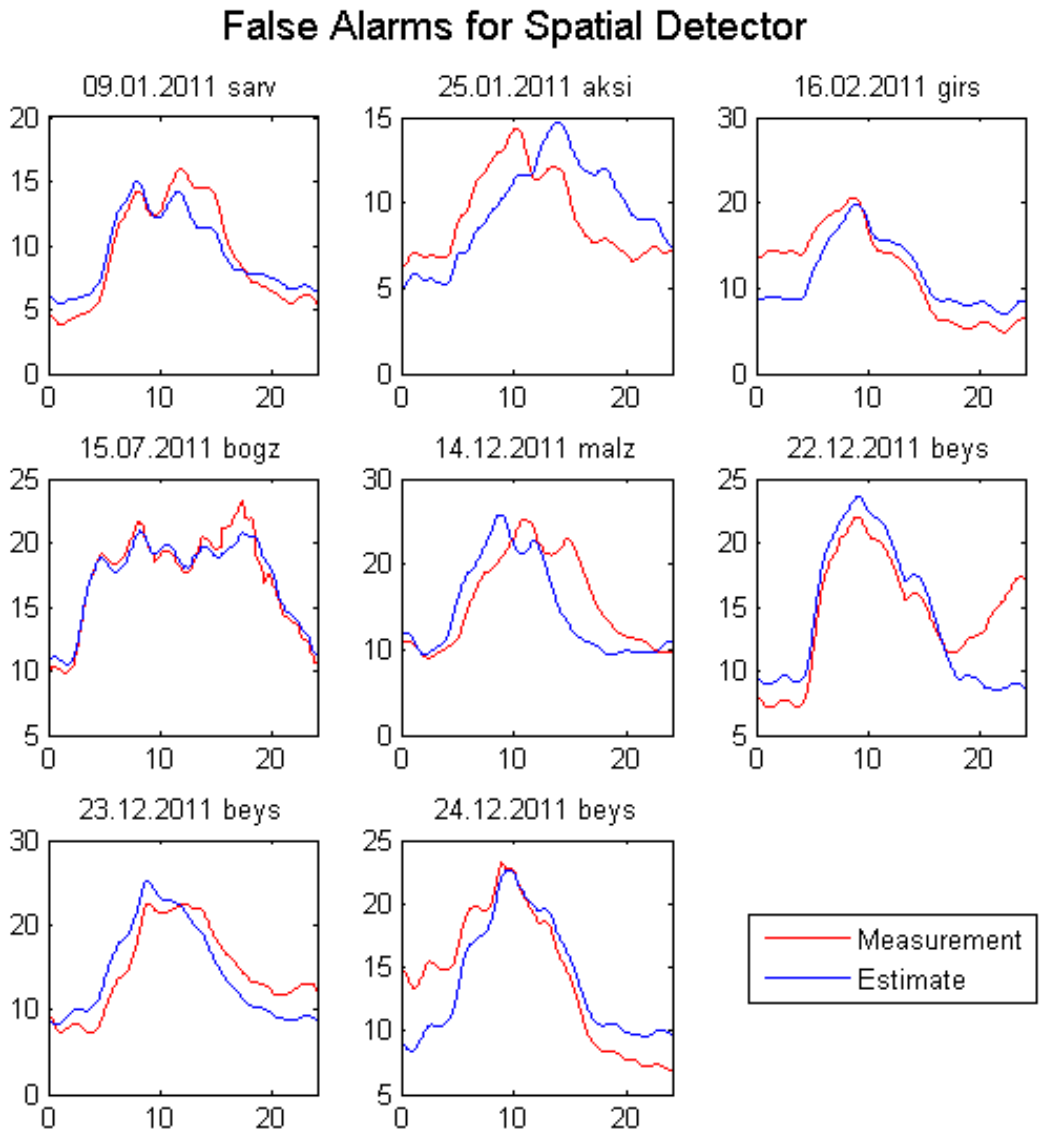

Figure 3.5: 8 different false alarm generating dates and 6 different false alarm regions: "sarv", "aksi", "girs", "bogz", "malz", and "beys" for combined daytime spatial earthquake detector.

As shown in Figure 3.4 and Figure 3.5, both combined detectors generate reasonable false alarms due to disturbances in TEC measurements and inconsistent TEC measurement estimates. For a false alarm date, false alarm regions are close to each other that mean value of the distance between false alarm regions for 8 false alarm days is $215.39km$.

Ionospheric TEC disturbances are not only triggered by solar radiation and

seismic activities but also affected by geomagnetic storms. Disturbance storm time (Dst) index is one of the widely used parameters for identifying geomagnetic storms [44]. The Dst index represents symmetric disturbed magnetic field on the Earth's surface. Negative Dst indices indicate amount of weakness observed on the Earth's magnetic field. The weakness of the Earth's magnetic field causes strong or weak geomagnetic storms in ionosphere with respect to the amount of the disturbance [45, 46]. Therefore, the effect of geomagnetic storms on the false alarm days shown in Figure 3.4 and Figure 3.5 is investigated. As given in Table 3.3, daily Dst indices for 7 out of 8 false alarm days are below zero indicating geomagnetic storms and 5 out of 8 false alarm days are below yearly median of the Dst index indicating strong geomagnetic storms. Dst indices are obtained from Kyoto Dst index service [47].

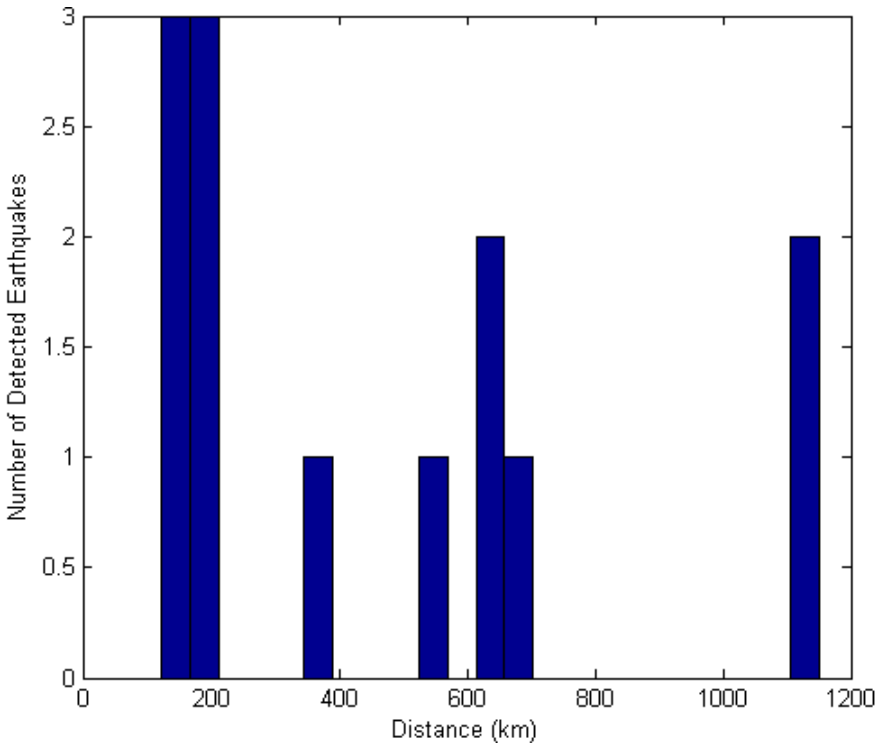

Figure 3.6: Earthquake detection distance for daytime fused earthquake detector.

Figure 3.6 illustrates histogram of the closest detection distances of the detected earthquakes with respect to the fused detector prediction result shown in Figure 3.3. Majority of the earthquakes are detected from distances smaller than $700km$ and 2 out of 13 earthquakes are detected from far distances higher than

$700km$. In the following section, another detection technique that reduces the effect of strong solar radiation on the ionospheric TEC variations is proposed.

3.3 Nighttime Results

Recent studies show the fact that current densities in the earthquake fault zone can cause Total Electron Content (TEC) variations of up to $2-25\%$ in daytime and $1-30\%$ in nighttime ionosphere [10]. Assuming ionospheric TEC variations are triggered by two main sources: strong solar radiation and seismic activities, ionospheric TEC variations are triggered by both solar radiation and seismic activities in daytime. However, seismic activities are the only main disturbing

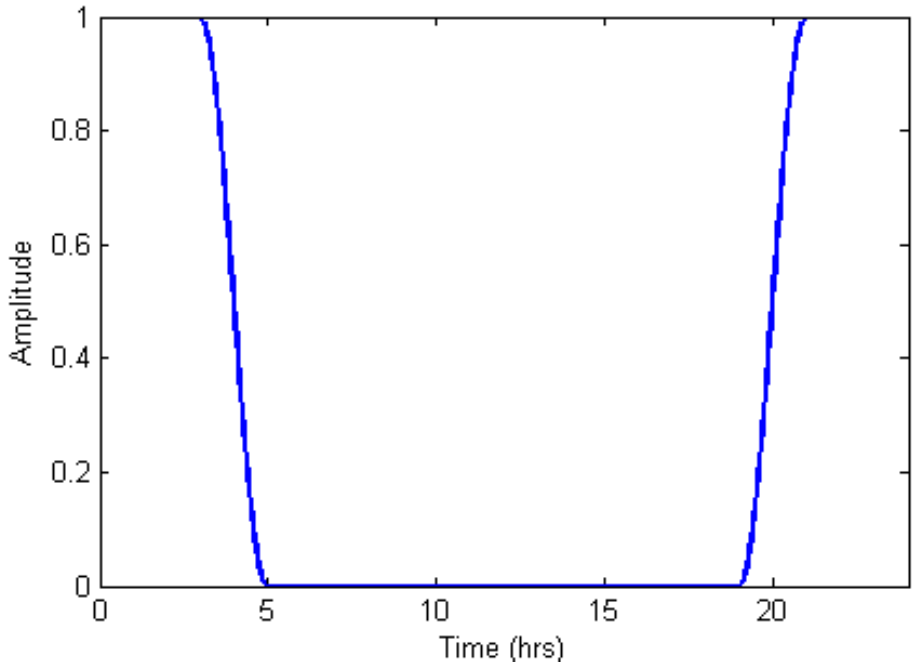

Figure 3.7: TEC measurement window function for generating nighttime TEC measurements.

sources of ionospheric TEC in nighttime. Therefore, wide range of TEC variations are observed in nighttime triggered by seismic activities and should be investigated by eliminating the effect of solar radiation on ionospheric TEC. To

eliminate the effect of solar radiation on ionospheric TEC variation, a simple TEC measurement window function is proposed in Figure 3.7. For a chosen TEC measurement, proposed window represses the effect of the solar radiation on the chosen TEC measurement from 5 am to 7 pm. Figure 3.8, illustrates two nighttime TEC measurements obtained by applying the window function for the TEC measurements shown in Figure 2.2.

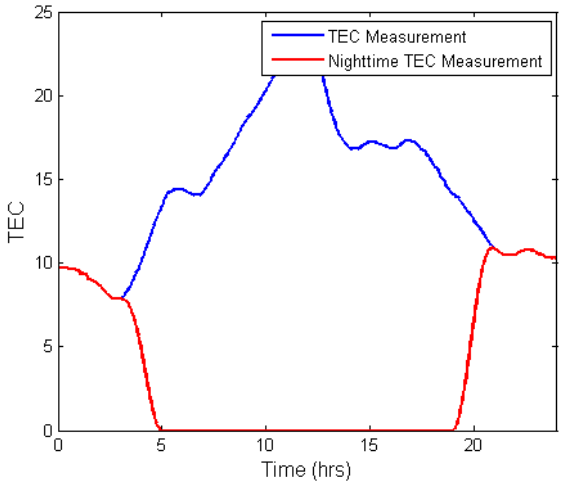

(a)

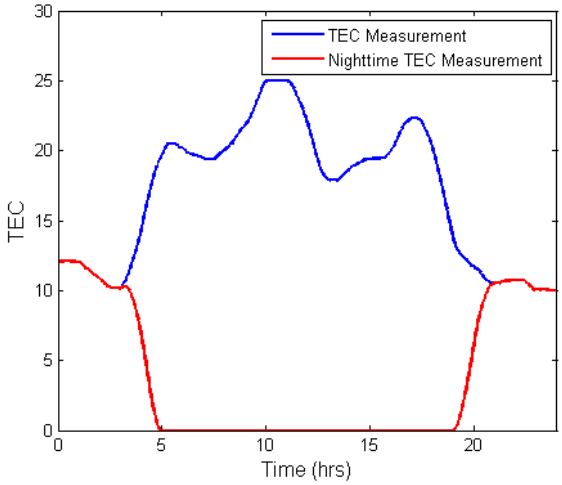

(b)

Figure 3.8: TEC measurements and nighttime TEC measurements at station "deni" on two different dates: (a) 21.04.2010 and (b) 23.04.2010.

Thereafter, proposed window is applied to all available TEC measurements, TEC estimates for these nighttime TEC measurements are obtained as discussed in Section 2.2, nighttime earthquake detection signals are generated as discussed

in Section 2.3, and appropriate earthquake detection thresholds are generated to control P_{FA}. Figure 3.9 visualizes ROC curves of temporal and spatial detectors with their fusion as discussed in Section 3.2 for nighttime TEC measurements.

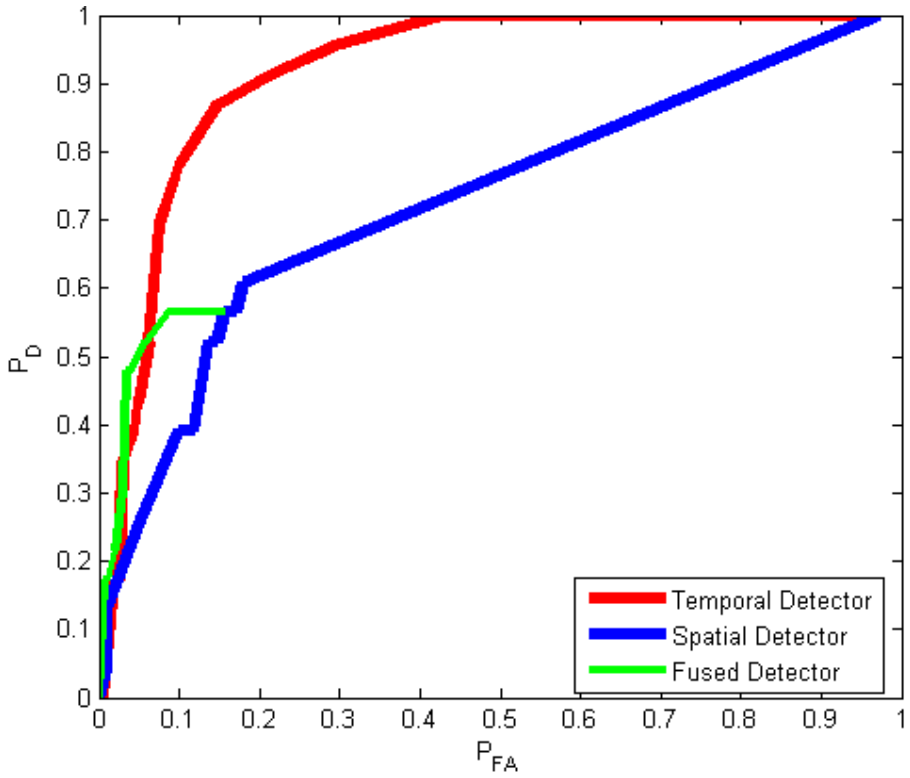

Figure 3.9: ROC curves of temporal (red), spatial (blue), and fused (green) earthquake detectors for nighttime earthquake detection signals.

To demonstrate particular performance of nighttime earthquake detection technique, a prediction result for fused detector is selected. The selected detects 11 out of 23 earthquakes while generating 7 false alarms. The earthquake prediction result for this detector is given in sixth column of Table 3.2. 7 of the earthquakes are detected by both daytime and nighttime fused detectors while nighttime fused detector detects 3 different earthquakes for the prediction results given in fourth and sixth columns of Table 3.2. Figure 3.10 and Figure 3.11 illustrate TEC measurements and their estimates for 7 false alarm generating regions of the fused detector prediction result shown in Figure 3.9. Figure 3.10 illustrates false alarms of combined temporal detector and Figure 3.11 illustrates false alarms of combined spatial detector for the date pairs of fused detector.

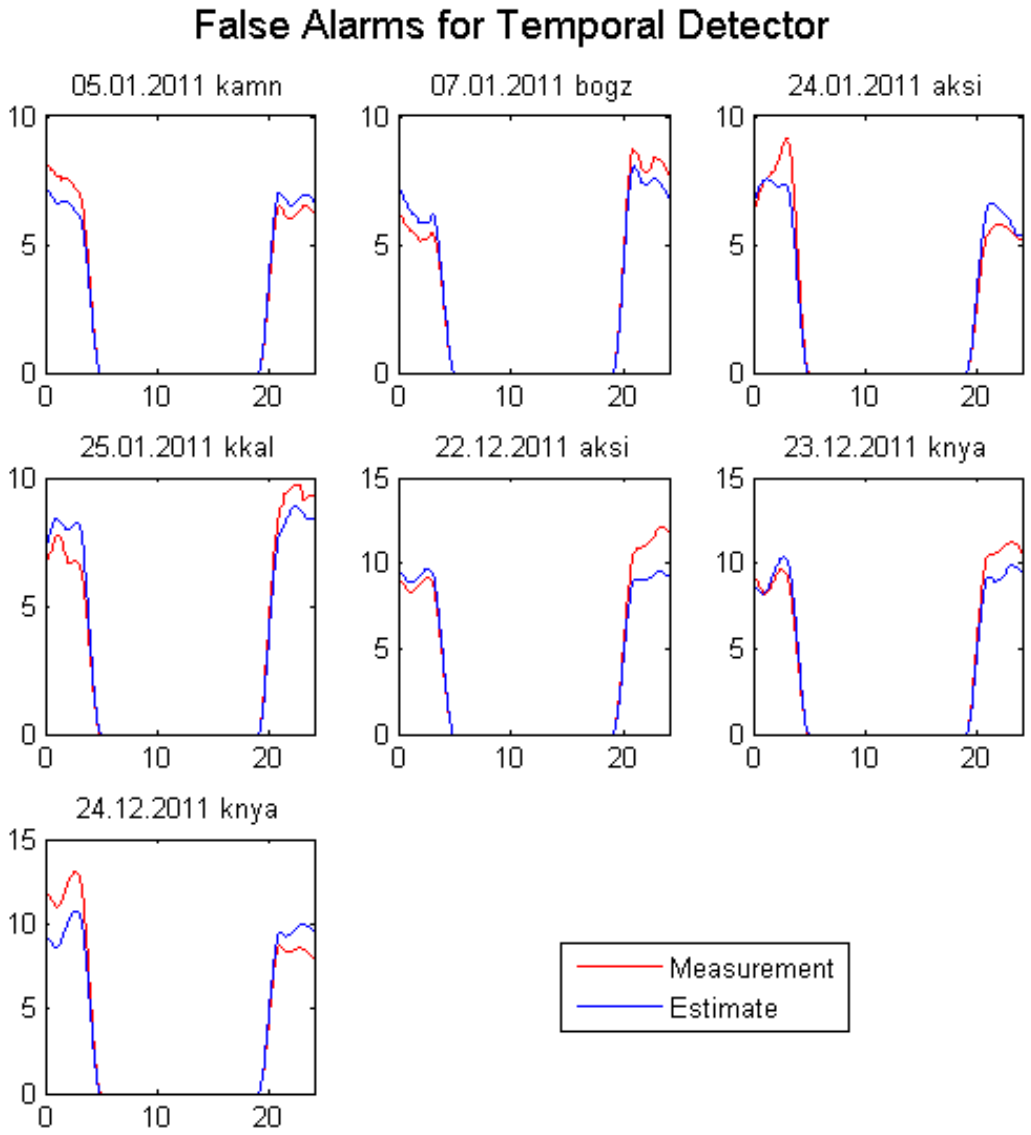

Figure 3.10: 7 different false alarm generating dates and 5 different false alarm regions: "kamn", "bogz", "aksi", "kkal", and "knya" for combined nighttime temporal earthquake detector.

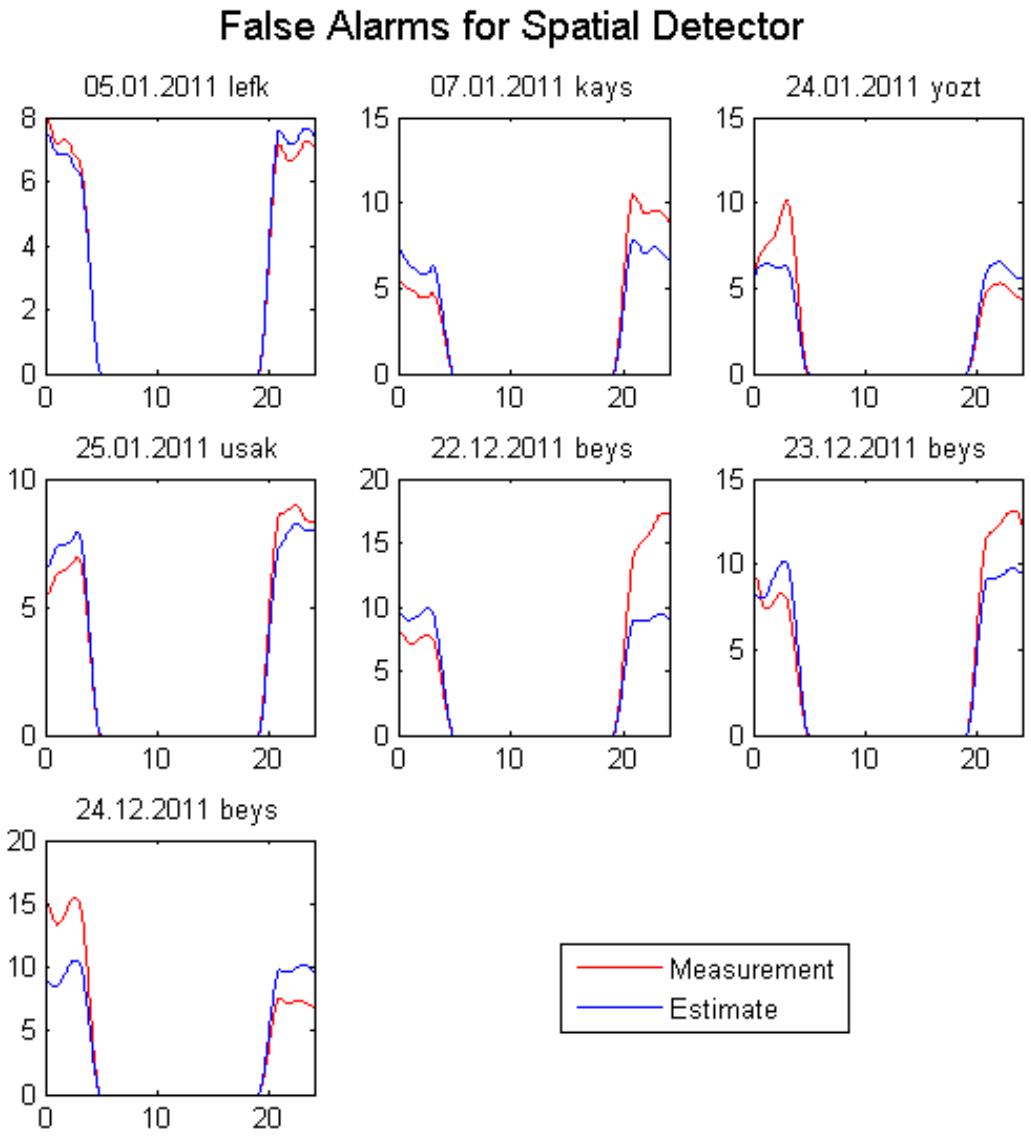

Figure 3.11: 7 different false alarm generating dates and 5 different false alarm regions: "lefk", "kays", "yozt", "usak", and "beys" for combined nighttime spatial earthquake detector.

As shown in Figure 3.10 and Figure 3.11, both combined detectors generate reasonable false alarms due to disturbances in TEC measurements and inconsistent TEC measurement estimates. For a false alarm date, false alarm regions are close to each other that mean value of the distance between false alarm regions for 7 false alarm days is $184.05km$. Also effect of geomagnetic storms on the false alarm days shown in Figure 3.10 and Figure 3.11 is investigated. As given in Table 3.3, daily Dst indices for 6 out of 7 false alarm days are below zero indicating

geomagnetic storms and 4 out of 7 false alarm days are below yearly median of the Dst index indicating strong geomagnetic storms.

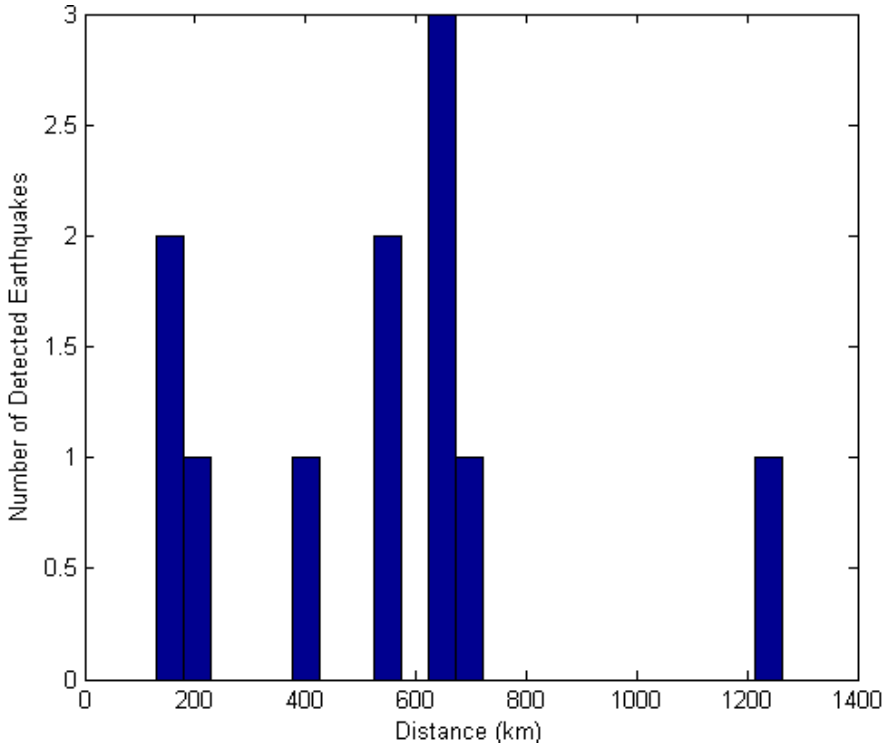

Figure 3.12: Earthquake detection distance for nighttime fused earthquake detector.

Figure 3.12 illustrates histogram of the closest detection distances of the detected earthquakes with respect to the fused detector prediction result shown in Figure 3.9. Majority of the earthquakes are detected from distances smaller than $700km$ and 1 out of 11 earthquakes is detected from a far distances higher than $700km$.

As shown in Figure 3.3 and Figure 3.9, nighttime temporal detector outperforms not only nighttime spatial detector but also daytime temporal and spatial detectors by achieving higher detection rates while operating fewer false alarm rates. Additionally, daytime spatial detector precedes nighttime spatial detector when P_{FA} is above 0.6. So as to achieve higher performance, nighttime temporal detector and daytime spatial detector are fused. Figure 3.13 visualizes ROC curves for nighttime temporal, daytime spatial and daytime-nighttime fused detector.

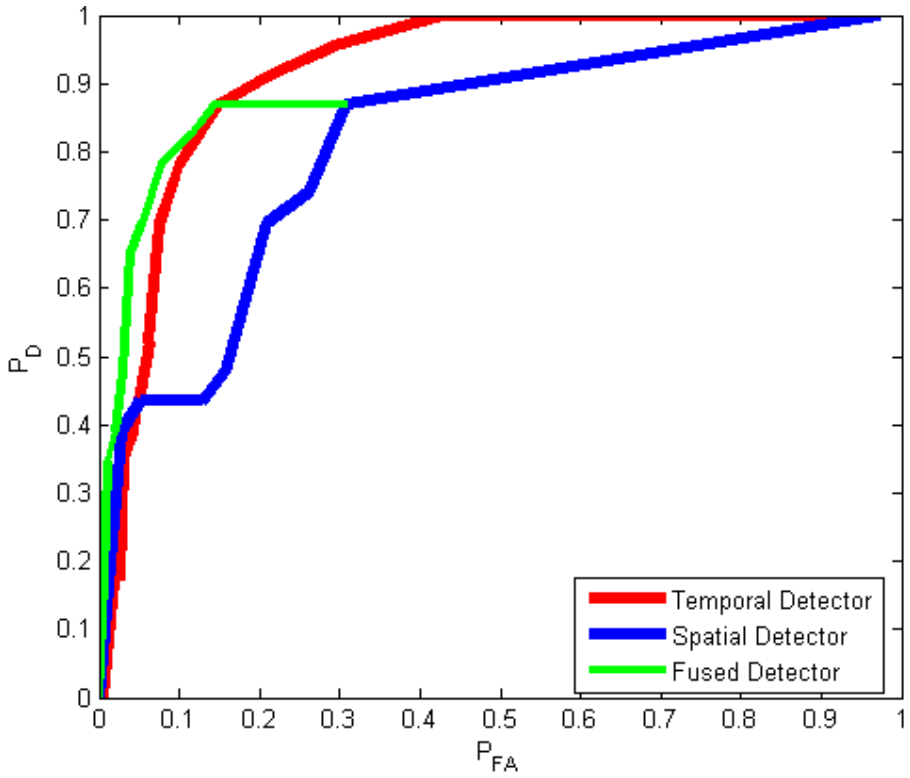

Figure 3.13: ROC curves for nighttime temporal (red), daytime spatial (blue), and daytime-nighttime fused (green) earthquake detectors.

To demonstrate particular performance of daytime-nighttime fused earthquake detector, a prediction result for fused detector is selected. The selected detects 15 out of 23 earthquakes while generating 8 false alarms. The earthquake prediction result for this detector is given in seventh column of Table 3.2. 12 of the earthquakes are detected by both daytime fused and daytime-nighttime fused detector while daytime-nighttime fused detector detects 3 different earthquakes for the prediction results given in fourth and seventh columns of Table 3.2. Figure 3.14 and Figure 3.15 illustrate TEC measurements and their estimates for 8 false alarm generating regions of the fused detector prediction result shown in Figure 3.13. Figure 3.14 illustrates false alarms of combined nighttime temporal detector and Figure 3.15 illustrates false alarms of combined daytime spatial detector for the date pairs of fused detector.

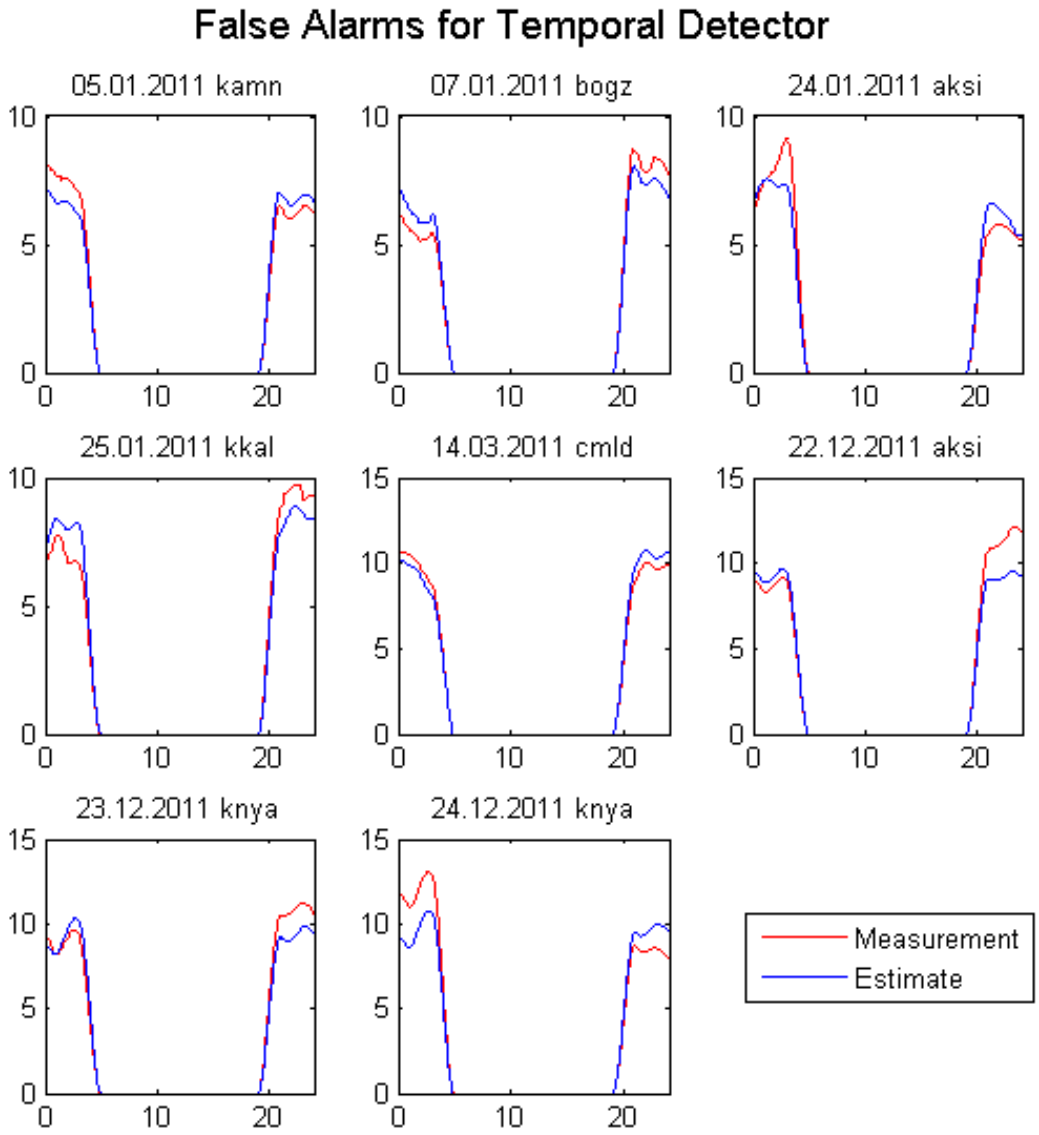

Figure 3.14: 8 different false alarm generating dates and 6 different false alarm regions: "kamn", "bogz", "aksi", "kkal", "cmld", and "knya" for combined nighttime temporal earthquake detector.

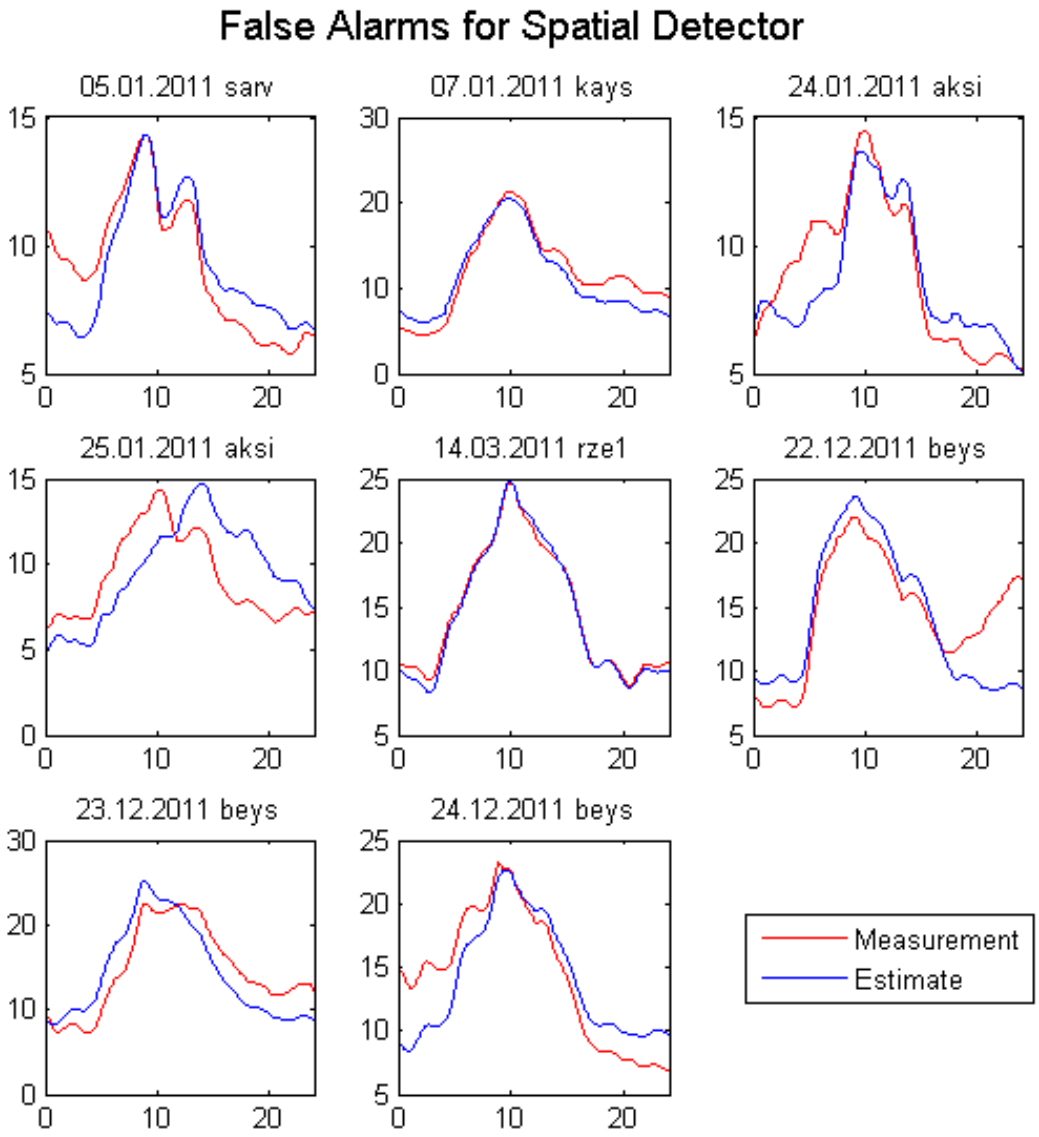

Figure 3.15: 8 different false alarm generating dates and 5 different false alarm regions: "sarv", "kays", "aksi", "rze1", and "beys" for combined daytime spatial earthquake detector.

As shown in Figure 3.14 and Figure 3.15, both combined detectors generate reasonable false alarms due to disturbances in TEC measurements and inconsistent TEC measurement estimates. For a false alarm date, false alarm regions are close to each other that mean value of the distance between false alarm regions for 8 false alarm days is 173.02km. Also effect of geomagnetic storms on the false alarm days shown in Figure 3.14 and Figure 3.15 is investigated. As given in Table 3.3, daily Dst indices for 7 out of 8 false alarm days are below zero indicating

geomagnetic storms and 6 out of 8 false alarm days are below yearly median of the Dst index indicating strong geomagnetic storms.

Figure 3.16 illustrates histogram of the closest detection distances of the detected earthquakes with respect to the fused detector prediction result shown in Figure 3.13. Majority of the earthquakes are detected from distances smaller than $700km$ and 2 out of 15 earthquakes are detected from far distances higher than $700km$.

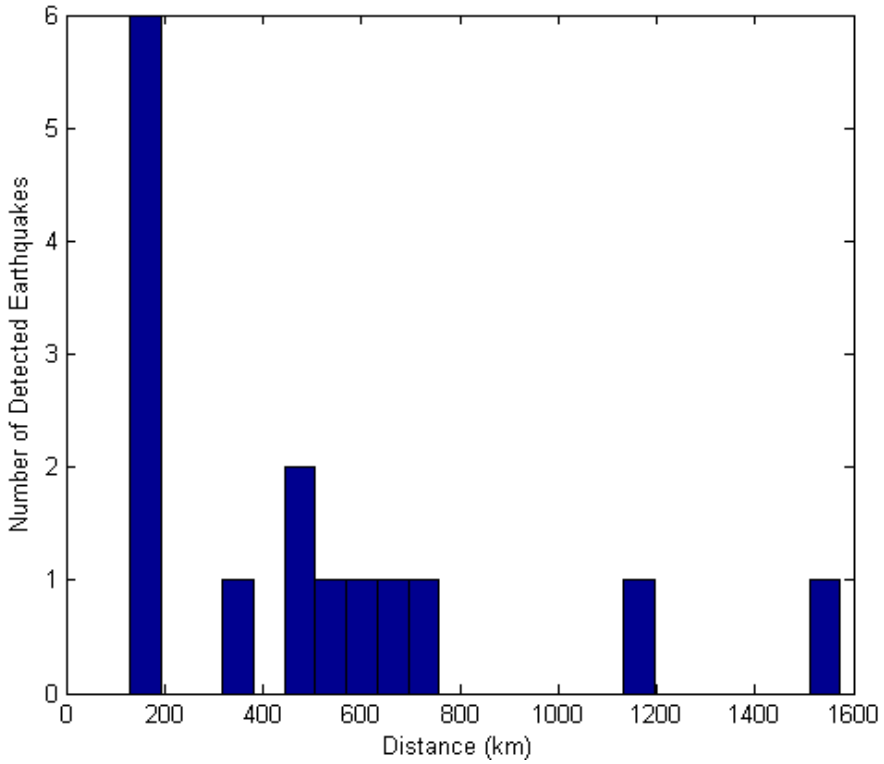

Figure 3.16: Earthquake detection distance for daytime-nighttime fused earthquake detector.

Table 3.2: 6 different detector earthquake prediction results for the 23 earthquakes. Detected earthquakes are marked as "1"s and missed earthquakes are marked as "0"s.

Date	Daytime				Nighttime	Best
(dd.mm.yyyy)	Temporal	Spatial	Fused	Fused	Fused	Fused
19.01.2011	0	1	0	1	0	0
28.02.2011	1	1	1	1	1	1
01.04.2011	0	0	0	0	0	0
19.05.2011	0	0	0	0	1	1
23.06.2011	0	0	0	0	0	0
27.06.2011	0	0	0	0	0	0
25.07.2011	1	0	1	0	1	1
18.08.2011	0	1	0	1	1	1
13.09.2011	1	1	1	1	1	1
14.09.2011	1	1	1	1	1	1
22.09.2011	0	0	0	0	0	0
27.09.2011	0	0	0	0	0	0
10.10.2011	1	0	1	0	0	0
23.10.2011	1	0	1	0	0	1
24.10.2011	1	0	1	0	0	1
25.10.2011	1	0	1	0	0	1
27.10.2011	1	0	1	0	0	1
08.11.2011	1	1	1	1	1	1
09.11.2011	1	1	1	1	1	1
14.11.2011	1	1	1	1	1	1
18.11.2011	1	1	1	1	1	1
23.11.2011	0	0	0	0	1	1
30.11.2011	0	0	0	0	0	0
Probability of Detection	13/23	9/23	13/23	9/23	11/23	15/23

3.4 Future Works

One of the main future works about the proposed earthquake detection approach is the addition of other ionospheric parameters such as Dst into detectors' earthquake decision process. When the Dst indices of investigated false alarm days in Figures 3.4-3.5, Figures 3.10-3.11, and Figures 3.14-3.15 are taken into consideration, state of the ionosphere is unstable due to geomagnetic storms for majority of these false alarm days as given in Table 3.3. Therefore, generated false alarms can be attributed to unstable condition of the ionosphere and eliminated by adding Dst index into detectors' earthquake decision process.

Table 3.3: Dst indices for false alarm days.

Date (dd.mm.yyyy)	Dst (nT)
05.01.2011	-0.33333
07.01.2011	-24.625
09.01.2011	-10.2917
24.01.2011	4.75
25.01.2011	-5.7083
16.02.2011	-10.2083
14.03.2011	-10.125
15.07.2011	5.4583
14.12.2011	-4.75
22.12.2011	-13.7083
23.12.2011	-5.25
24.12.2011	-2.0417
2011 Median : -4.7917	

On the other hand, effect of Dst indices on earthquake decision process should be investigated for the earthquake detection days that it may not possible to detect earthquakes due to unstable ionospheric state triggered by strong geomagnetic storms. Table 3.4, Table 3.5, and Table 3.6 give earthquake decision dates with their Dst indices and number of observed ionospheric anomalies before the earthquakes take place for the earthquake prediction results shown in the fourth, sixth, and seventh columns of Table 3.2, respectively.

Table 3.4: Daytime fused detector prediction result for 13 detected earthquakes with number of observed anomalies, earthquake decision date, and earthquake decision date Dst index.

Daytime Fused Detector Prediction Result			
Earthquake Date (dd.mm.yyyy)	Observed Anomalies	Decision Date (dd.mm.yyyy)	Dst (nT)
28.02.2011	5	25.02.2011	4.5
25.07.2011	6	16.07.2011	3.833
13.09.2011	5	08.09.2011	3.833
14.09.2011	5	08.09.2011	3.833
10.10.2011	5	08.10.2011	6.375
23.10.2011	2	22.10.2011	3.375
24.10.2011	2	22.10.2011	3.375
25.10.2011	2	22.10.2011	3.375
27.10.2011	2	22.10.2011	3.375
08.11.2011	2	06.11.2011	-0.833
09.11.2011	2	06.11.2011	-0.833
14.11.2011	4	12.11.2011	-0.25
18.11.2011	4	12.11.2011	-0.25

Table 3.5: Nighttime fused detector prediction result for 11 detected earthquakes with number of observed anomalies, earthquake decision date, and earthquake decision date Dst index.

Nighttime Fused Detector Prediction Result			
Earthquake Date (dd.mm.yyyy)	Observed Anomalies	Decision Date (dd.mm.yyyy)	Dst (nT)
28.02.2011	5	25.02.2011	4.5
19.05.2011	2	14.05.2011	8.083
25.07.2011	2	24.07.2011	-4.458
18.08.2011	2	18.08.2011	-0.208
13.09.2011	1	06.09.2011	-7.958
14.09.2011	1	06.09.2011	-7.958
08.11.2011	2	06.11.2011	-0.833
09.11.2011	2	06.11.2011	-0.833
14.11.2011	3	12.11.2011	-0.25
18.11.2011	5	12.11.2011	-0.25
18.11.2011	4	16.11.2011	-1.666

As shown in Table 3.4, adding Dst index into daytime fused detector earthquake decision process will not affect number of detected earthquakes due to multiple observed anomalies before the earthquakes take place and Dst indices of which are positive or close to zero. However, 2 out of 11 earthquakes will not be declared as detected for the prediction result of nighttime fused detector that there is no other observed ionospheric anomaly other than anomalies on decision dates and Dst indices on the decision dates are indicating strong geomagnetic storms. Therefore, adding Dst index into nighttime fused detector earthquake decision process affects number of detected earthquakes as shown in Table 3.5.

Table 3.6: Daytime-Nighttime fused detector prediction result for 15 detected earthquakes with number of observed anomalies, earthquake decision date, and earthquake decision date Dst index.

Daytime-Nighttime Fused Detector Prediction Result			
Earthquake Date (dd.mm.yyyy)	Observed Anomalies	Decision Date (dd.mm.yyyy)	Dst (nT)
28.02.2011	4	25.02.2011	4.5
19.05.2011	2	14.05.2011	8.083
25.07.2011	5	16.07.2011	3.833
18.08.2011	6	18.08.2011	-0.208
13.09.2011	5	08.09.2011	3.833
14.09.2011	5	08.09.2011	3.833
23.10.2011	2	22.10.2011	3.375
24.10.2011	2	22.10.2011	3.375
25.10.2011	2	22.10.2011	3.375
27.10.2011	2	22.10.2011	3.375
08.11.2011	2	06.11.2011	-0.833
09.11.2011	2	06.11.2011	-0.833
14.11.2011	4	12.11.2011	-0.25
18.11.2011	4	12.11.2011	-0.25
23.11.2011	2	18.11.2011	-0.25

Furthermore, adding Dst index into daytime-nighttime fused detector earthquake decision process will not affect number of detected earthquakes due to multiple observed anomalies before the earthquakes take place and Dst indices of which are positive or close to zero as shown in Table 3.6. Therefore, addition of Dst parameter into the proposed earthquake detection approach suggests the possibility of reducing geomagnetic storm triggered false alarms while not affecting

earthquake detections.

As an another future work, active fault lines can be integrated into the proposed earthquake detection approach to eliminate false alarms away from the active fault lines. Hereby robust detection of earthquakes with earthquake epicenter and time becomes possible.

Also, a new decision fusion technique can be developed by fusing other earthquake detectors or ionospheric parameters for improved performance.

Chapter 4

CONCLUSIONS AND FUTURE RESEARCH

Ionosphere is an atmosphere layer where predictable daily and seasonal alterations occur due to position of the Sun and unpredictable and rapid alterations occur due to solar radiation, geomagnetic activity, seismic and gravitational variations. Recent studies show the fact that ionosphere is not only affected by strong solar radiation and geomagnetic activities but also affected by seismic activities resulting with strong earthquakes.

Due to the lack of statistical reliability analysis of earthquake precursors, earthquake prediction from ionospheric parameters is considered to be controversial. In this thesis, reliability of earthquake prediction based on detection of local ionospheric anomalies is investigated using dense TEC data obtained from the Turkish National Permanent GPS Network (TNPGN-Active).

In order to unveil local ionospheric anomalies, an earthquake detection signal is generated based on the distance between TEC measurements and their estimates. By applying a novel spatio-temporal TEC interpolation technique, TEC measurement estimates that are adhere to sunspot numbers are obtained. Two different detectors: spatial and temporal earthquake detectors that are generated based on the statistics obtained form the earthquake detection signal are proposed

for the robust detection of earthquake based local TEC anomalies. Performances of the proposed detectors are evaluated for the 23 earthquakes occurred around Turkey with magnitude greater or equal than 5 in Richter scale during 2011. It is observed that false alarms generated by deployed detectors are scattered around Turkey and highly uncorrelated. Hence, a detector fusion technique is proposed for achieving higher performance in terms of lower false alarm and higher detection rates. Results indicate that fused detectors can detect the same number of earthquakes as deployed spatial and temporal detectors while generating fewer number of false alarms.

Furthermore, nighttime TEC varaitions are investigated by eliminating the effect of solar radiation on ionospheric TEC. To eliminate the effect of solar radiation on ionospheric TEC variation, a simple TEC measurement window function is proposed and applied to TEC measurements to obtain nighttime earthquake detection signal. Nighttime earthquake detection provides different prediction results compared to daytime results. Finally, another fused detector is deployed to both daytime and nighttime earthquake detection signals. It is observed that the daytime-nighttime fused detection has superior performance and able to detect 15 out of 23 earthquakes while generating 8 false alarms but there is still room for improvement. Obtained results suggest that there is a strong possibility of earthquake detection by monitoring local TEC variations.

As future works, the position of active faults can be included to the decision logic by eliminating threshold exceedences away from the active fault lines. Region and time based detectors should be generated for the accurate detection of earthquake epicenter and time, respectively. As indicated in Section 3.4, addition of Dst parameter into the proposed earthquake detection approach suggests the possibility of reducing geomagnetic storm triggered false alarms. Also, a new decision fusion technique can be developed by fusing other earthquake detectors for improved performance.

Bibliography

[1] H. Nayir, "Ionospheric Total Electron Content Estimation Using GPS Signals," Master's thesis, Hacettepe University, 2007.

[2] A. Komjathy, *Global ionospheric total electron content mapping using the Global Positioning System*. PhD thesis, University of New Brunswick, New Brunswick, Canada, 1997.

[3] G. Guo and B. Wang, "Cloud anomaly before Iran earthquake," *International Journal of Remote Sensing*, vol. 29, no. 7, pp. 1921–1928, 2008.

[4] S. Pulinets, D. Ouzounov, A. Karelin, K. Boyarchuk, and L. Pokhmelnykh, "The physical nature of thermal anomalies observed before strong earthquakes," *Physics and Chemistry of the Earth, Parts A/B/C*, vol. 31, no. 4, pp. 143–153, 2006.

[5] A. A. Tronin, M. Hayakawa, and O. A. Molchanov, "Thermal IR satellite data application for earthquake research in Japan and China," *Journal of Geodynamics*, vol. 33, no. 4, pp. 519–534, 2002.

[6] A. Tronin, P. Biagi, O. Molchanov, Y. Khatkevich, and E. Gordeev, "Temperature variations related to earthquakes from simultaneous observation at the ground stations and by satellites in Kamchatka area," *Physics and Chemistry of the Earth, Parts A/B/C*, vol. 29, no. 4, pp. 501–506, 2004.

[7] C. Fidani, "The earthquake lights (EQL) of the 6 April 2009 Aquila earthquake, in Central Italy," *Nat. Hazards Earth Syst. Sci*, vol. 10, no. 5, pp. 967–978, 2010.

[8] M. Ikeya, *Earthquakes and Animals: From Folks Legends to Science*. World Scientific, 2004.

[9] F. Freund, "Cracking the Code of Pre-Earthquake Signals," *National Information Service for Earthquake Engineering, University of California, Berkeley*, 2005.

[10] C. Kuo, J. Huba, G. Joyce, and L. Lee, "Ionosphere plasma bubbles and density variations induced by pre-earthquake rock currents and associated surface charges," *Journal of Geophysical Research*, vol. 116, no. A10, p. A10317, 2011.

[11] D. Ouzounov, S. Pulinets, A. Romanov, A. Romanov, K. Tsybulya, D. Davidenko, M. Kafatos, and P. Taylor, "Atmosphere-ionosphere response to the M9 Tohoku earthquake revealed by multi-instrument space-borne and ground observations: Preliminary results," *Earthquake Science*, vol. 24, no. 6, pp. 557–564, 2011.

[12] A. Namgaladze, O. Zolotov, I. Zakharenkova, I. Shagimuratov, and O. Martynenko, "Ionospheric total electron content variations observed before earthquakes: Possible physical mechanism and modeling," *arXiv preprint arXiv:0905.3313*, 2009.

[13] S. Pulinets, "Seismic activity as a source of the ionospheric variability," *Advances in Space Research*, vol. 22, no. 6, pp. 903–906, 1998.

[14] V. Plotkin, "GPS detection of ionospheric perturbation before the 13 February 2001, El Salvador earthquake," *Natural Hazards and Earth System Science*, vol. 3, no. 3/4, pp. 249–253, 1999.

[15] A. Trigunait, M. Parrot, S. Pulinets, F. Li, *et al.*, "Variations of the ionospheric electron density during the Bhuj seismic event," in *Annales Geophysicae*, vol. 22, pp. 4123–4131, 2004.

[16] S. Pulinets, A. Kotsarenko, L. Ciraolo, and I. Pulinets, "Special case of ionospheric day-to-day variability associated with earthquake preparation," *Advances in Space Research*, vol. 39, no. 5, pp. 970–977, 2007.

[17] S. Pulinets, A. Leyva-Contreras, G. Bisiacchi-Giraldi, and C. Ciraolo, "Total electron content variations in the ionosphere before the Colima, Mexico, earthquake of 21 January 2003," *Geofísica Internacional*, vol. 44, no. 4, 2005.

[18] S. Pulinets, "Ionospheric precursors of earthquakes; recent advances in theory and practical applications," *Terrestrial Atmospheric and Oceanic Sciences*, vol. 15, no. 3, pp. 413–436, 2004.

[19] S. Pulinets, T. Gaivoronska, A. L. Contreras, L. Ciraolo, *et al.*, "Correlation analysis technique revealing ionospheric precursors of earthquakes," *Natural Hazards and Earth System Science*, vol. 4, no. 5/6, pp. 697–702, 2004.

[20] M. Zhang, J. Shi, X. Wang, and S. Radicella, "Ionospheric variability at low latitude station: Hainan, China," *Advances in Space Research*, vol. 34, no. 9, pp. 1860–1868, 2004.

[21] J. Liu, Y. Chen, S. Pulinets, Y. Tsai, and Y. Chuo, "Seismo-ionospheric signatures prior to M$\geq$ 6.0 Taiwan earthquakes," *Geophysical research letters*, vol. 27, no. 19, pp. 3113–3116, 2000.

[22] J. Y. Liu, Y. Chuo, S. Shan, Y. Tsai, Y. Chen, S. Pulinets, S. Yu, *et al.*, "Pre-earthquake ionospheric anomalies registered by continuous GPS TEC measurements," in *Annales Geophysicae*, vol. 22, pp. 1585–1593, 2004.

[23] L. Ciraolo and P. Spalla, "A statistics of time and space variability of ionospheric electron content at middle latitudes," *XXVI General Assembly URSI*, pp. 13–21, 1999.

[24] S. Kouris, K. Polimeris, and L. R. Cander, "Specifications of TEC variability," *Advances in Space Research*, vol. 37, no. 5, pp. 983–1004, 2006.

[25] S. Kouris and D. Fotiadis, "Ionospheric variability: a comparative statistical study," *Advances in Space Research*, vol. 29, no. 6, pp. 977–985, 2002.

[26] A. Yildiz, O. Arikan, and F. Arikan, "Spatio-temporal interpolation of ionospheric TEC data," in *IEEE 19th Conference on Signal Processing and Communications Applications (SIU)*, pp. 817–820, 2011.

[27] M. N. Deviren, F. Arikan, and O. Arikan, "Spatio-temporal interpolation of total electron content using a GPS network," *Radio Science*, pp. n/a–n/a, 2013.

[28] F. Arikan, C. Erol, and O. Arikan, "Regularized estimation of vertical total electron content from Global Positioning System data," *Journal of Geophysical Research*, vol. 108, no. A12, p. 1469, 2003.

[29] "IONOLAB, Ionospheric Research Laboratory." http://www.ionolab.org/. Accessed: 2013-07-15.

[30] "SIDC, Solar Influences Data Analysis Center." http://sidc.oma.be/sunspot-data/dailyssn.php. Accessed: 2013-07-15.

[31] T. M. Cover and J. A. Thomas, *Elements of information theory*. John Wiley & Sons, 2012.

[32] P. Hall, "On Kullback-Leibler loss and density estimation," *The Annals of Statistics*, vol. 15, no. 4, pp. 1491–1519, 1987.

[33] J. Inglada, "Change detection on SAR images by using a parametric estimation of the Kullback-Leibler divergence," in *Proceedings of IEEE International Geoscience and Remote Sensing Symposium, IGARSS'03*, vol. 6, pp. 4104–4106, 2003.

[34] N. Türel, "Power Spectral Density and Probability Density Function Estimation of the Total Electron Content of the Ionosphere Layer," Master's thesis, Hacettepe University, Ankara, 2008.

[35] S. Karatay, F. Arikan, and O. Arikan, "Investigation of Hourly and Daily Patterns for Lithosphere-Ionosphere Coupling Before Strong Earthquakes," *Recent Advances in Space Research*, 2009.

[36] M. L. Stein, *Interpolation of spatial data: some theory for kriging*. Springer, 1999.

[37] I. Stanislawska, G. Juchnikowski, L. R. Cander, L. Ciraolo, P. Bradley, Z. Zbyszynski, and A. Swiatek, "The kriging method of TEC instantaneous mapping," *Advances in Space Research*, vol. 29, no. 6, pp. 945–948, 2002.

[38] I. B. Aban, M. M. Meerschaert, and A. K. Panorska, "Parameter estimation for the truncated Pareto distribution," *Journal of the American Statistical Association*, vol. 101, no. 473, pp. 270–277, 2006.

[39] B. C. Arnold, "Pareto and generalized pareto distributions," in *Modeling Income Distributions and Lorenz Curves*, pp. 119–145, Springer, 2008.

[40] L. Zaninetti and M. Ferraro, "On the truncated Pareto distribution with applications," *Central European Journal of Physics*, vol. 6, no. 1, pp. 1–6, 2008.

[41] C. Xia, S. Yang, G. Xu, B. Zhao, and T. Yu, "Ionospheric anomalies observed by GPS TEC prior to the Qinghai-Tibet region earthquakes," *Terr. Atmos. Ocean. Sci*, vol. 22, no. 2, pp. 177–185, 2011.

[42] X. Zhang, X. Shen, and Y. Miao, "Electromagnetic Anomalies around Wenchuan Earthquake and Their Relationship with Earthquake Preparation," *Procedia Environmental Sciences*, vol. 12, pp. 693–701, 2012.

[43] W. Elmenreich, "A review on system architectures for sensor fusion applications," in *Software Technologies for Embedded and Ubiquitous Systems*, pp. 547–559, Springer, 2007.

[44] M. Sugiura, T. Kamei, A. Berthelier, and M. Menvielle, *Equatorial Dst Index: 1957-1986*. ISGI Publications Office, 1991.

[45] S.-I. Akasofu and S. Chapman, "On the asymmetric development of magnetic storm fields in low and middle latitudes," *Planetary and Space Science*, vol. 12, no. 6, pp. 607–626, 1964.

[46] M. Sugiura and S. Chapman, "The average morphology of geomagnetic storms with sudden commencement," tech. rep., DTIC Document, 1961.

[47] "Geomagnetic Equatorial Dst index Home Page." http://wdc.kugi.kyoto-u.ac.jp/dstdir/index.html. Accessed: 2013-04-08.